UNIVERSITY OF OKLAHOMA

GRADUATE COLLEGE

IMPROVEMENT AND CHARACTERIZATION OF DIRECT-INK-WRITE MANUFACTURED CONTINUOUS FIBER REINFORCED PHOTOPOLYMER MATRIX COMPOSITES

A THESIS

SUBMITTED TO THE GRADUATE FACULTY

In partial fulfillment of the requirements for

Degree of

MASTER OF SCIENCE

By

PETER SANDELL
Norman, Oklahoma
2023

IMPROVEMENT AND CHARACTERIZATION OF DIRECT-INK-WRITE MANUFACTURED CONTINUOUS FIBER REINFORCED PHOTOPOLYMER MATRIX COMPOSITES

A THESIS APPROVED FOR THE

SCHOOL OF AEROSPACE AND MECHANICAL ENGINEERING

BY THE COMMITTEE CONSISTING OF

Dr. Yingtao Liu, Chair

Dr. Kuang-Hua Chang

Dr. Dong Zhang

Acknowledgements

I must first extend my gratitude to Dr. Yingtao Liu for his constant support for, and dedication to, the SMIS lab and his students. During these past two years, I have been able to push my ideas to the limit and gain genuine engineering experience, all under expert guidance. I also cannot thank him enough for his trust, patience, and assistance as I balanced many responsibilities during my graduate studies. I would also like to thank Dr. Kuang-Hua Chang and Dr. Dong Zhang for generously lending me their time and expertise as members of my thesis committee.

I would next like to formally acknowledge the previous work of Ryan Cowdrey, who designed and built the first iteration of the printer I later augmented. Although I altered many aspects of it, the system still operates on the same underlying principles which he first actualized.

Among other faculty members, I am especially grateful to Dr. Ramkumar Parthasarathy and Dr. Thomas Hays for teaching me how to build planes. I consider myself very lucky to have been at OU when I could benefit from their experience and knowledge. I have especially appreciated Dr. Parthasarathy's friendliness and helpfulness throughout my time in Aerospace Engineering, even as his free time has continued to shrink.

Thank you also to my colleagues who made research enjoyable and always offered their help and ideas: Lane Taylor, Benjamin Sherwood, Steven Zhao, Daniel Fitzpatrick, Cameron Collum, Alene Basmadjian, Jacob Hering, and Anirban Mondal. I must especially note the help and friendship of Christopher Billings, who directly enabled several of my designs and taught me a lot about being an engineer. I have also had the

opportunity to learn exponentially more than I had ever hoped about manufacturing thanks to the help of Elijah Personette, Billy Mays, and Jimmy Cannon.

Finally, I cannot express my thanks enough to my family. I would not have been able to push this far without the sacrifices and dedication of my parents, and anything I do that I can call an accomplishment has been built upon their foundation. To my friends from beyond my time at OU, the Table, and especially Anthony for his advice in C++ wizardry, thank you for sticking with me. I could not ask for better people to have around as we all continue to push forward.

Table of Contents

Table of Figures

Table of Tables

Abstract

Fiber reinforced polymer (FRP) composites play a significant and continuously growing role in engineering applications that require high strength, weight optimized structural components. Additive manufacturing (AM) has proven to be an extremely powerful tool in expanding the limits of part complexity and optimization. The present work aims to combine the two by reliably and efficiently additively manufacturing continuous fiber reinforced thermoset polymer composites. Building off previous efforts, a novel 3D printer was refined that utilizes direct ink write (DIW) technology to simultaneously extrude both an in-situ cured UV resin and continuous reinforcing fiber. Improvements to the system ensured that the most common failures were significantly mitigated or eliminated. The capabilities of the printer, specifically the maximum print size, were also increased by a wide margin. The printer's more predictable state allowed the creation of samples for material characterization. Tensile specimens showed strengths as high as 209 MPa and an average tensile modulus of 19.5 MPa. Volume fraction testing using carbonization in a nitrogen atmosphere gave an average fiber volume fraction of 8.3%. These are competitive with the results of other investigations of similar continuous fiber AM processes. The printed material was further characterized with scanning electron microscopy, showing that the bonding between matrix layers and resin impregnation within fibers were both ideal. Printed cones and honeycombs also showed that the process can produce complex geometry. Future efforts can serve to increase the fiber volume fraction and overall strength optimization of the printed material. The introduction of new materials into the process, like fiberglass or nanoparticles, could also change the properties of the products to have better curing behavior or higher strength.

Chapter 1: Introduction

1.1 Uses, Types, and Manufacturing of Fiber Reinforced Polymer Composites

The role of fiber-reinforced polymer (FRP) composites in structural applications has seen growth in recent decades. This has been especially true in aerospace industries, where the exceptionally high strength-to-weight ratio of some composites makes them well suited replacements for metals [1-5]. High profile examples can be seen in the form of aircraft like the Boeing 787, where up to 80% of the aircraft has been built using FRP materials. This is a drastic change from only 50 years ago, when the sophisticated Concorde consisted of only 7% composite materials [6]. Small-scale applications of composite materials have also seen an explosion in both quantity and assortment of task. UAVs, ground vehicles, and ballistic protection industries have benefited from the light weight and high strength promised by fiber-reinforced composites [7-9].

As the diversity of applications has expanded, so too has the need for diversity in material characteristics. This has spurred the development of a wide array of fiber reinforced polymer matrix composites with variations in fiber size, fiber material, and matrix material. Those that see the lowest strength increase over that of the matrix employ thermoplastic or thermoset matrices and short fiber reinforcement. This formulation allows for simplified manufacturing in the form of injection molding, and alterations in fiber alignment and length can significantly change the directional strength characteristics of the final material [10, 11].

The highest strength FRP composites are composed of long fibers in a thermosetting matrix [11]. Although long fibers offer a significant performance benefit

over short fibers, their more elaborate manufacturing techniques have proven restrictive to their applications. Some of the most common practices are layups, resin transfer molding and vacuum-assisted resin transfer molding (RTM and VARTM), pultrusion, and filament winding. In layups, sheets of woven or unidirectional material are coated in thermosets and stacked by hand or with the assistance of machines. In RTM, resin is injected into a shaped and enclosed fabric. VARTM applies the same resin injection technique, but couples it with a vacuum force at the extremities of the part to better encourage the movement of resin and evacuate volatile gases during cure. Pultrusion takes wetted material and pulls it through a heated die to form long structural members. Finally, filament winding is used to create monolithic solids of revolution, like fuselages or other pressure vessels, by spinning a structure like a spool and strategically layering one or many threads on it as they are wrapped.

These common processes rely on different methods of curing including ovens, autoclaves, and simple room temperature curing for long periods of time. Autoclaves require significant real estate and machinery, as they both pressurize and heat the atmosphere around a part during cure. Unpressurized ovens are less intensive, although they once again require some form of heating chamber, commonly in addition to the floorspace used to assemble and prepare the composites before curing. Room temperature cure is simply time consuming, and most resins will benefit from some level of thermal cure, regardless.

Broadly speaking, these manufacturing techniques are achievable when necessary to take advantage of the significant benefits of composite materials. However, time, labor, specialized machinery, and floorspace are required at nearly every step of the way. Most

notably, modern methods have yet to produce more versatile manufacturing tools for long fiber thermoset matrix composites analogous to the CNC mills and lathes used to make analogous structures with metal or other machinable materials.

1.2 Additive Manufacturing Review

The complexity, cost, and inflexibility of widely available FRP manufacturing techniques have provided an impetus to search for better methods. Additive manufacturing, also known as 3D printing, has proven itself to provide rapid, economical solutions to nearly every aspect of production [12-23].

Additive manufacturing is divided into several categories that delineate between material deposition mechanisms. Common, commercially available 3D printers are used in conjunction with low-strength thermoplastics, like polylactic acid (PLA) and acrylonitrile butadiene (ABS), for rapid prototyping both in enthusiast and professional settings. Such machines are based on fused deposition modeling (FDM), in which a thermoplastic filament is melted in a heating chamber and extruded through a nozzle. Once the plastic is deposited, it quickly cools and forms a small layer of the final model. Most FDM uses 3-axis machining techniques to slice a model into layers and determine toolpaths. Extensions of FDM have been made that allow printing high-strength thermoplastics, like poly-ether-ether-ketone (PEEK) and nylon [13]. The mechanical properties of a few common FDM thermoplastics are given in Table 1 for future reference.

Table 1: Mechanical Properties of Common FDM Thermoplastics

Material	Tensile Modulus (GPa)	Tensile Strength at Yield (MPa)
PLA [24]	3.6	62
ABS [25]	2.4	43
Nylon [26]	2.2	66

Structural and specialty components can also be additively manufactured with metals. Metal processes are most commonly based on powder bed fusion (PBF) technology. Components are built up by layering and melting fine metal powder with a laser to form solid metal. PBF has so far played a limited role in industry applications, mostly in aerospace [27-29].

The additive process most relevant to the present work is direct ink write (DIW), which has extremely wide-ranging applications. Any viscous liquid can be pressurized and deposited via a nozzle either into a substrate or onto a platform. DIW has been used for ceramics, polymers, gels, self-sensing composites, and even food. It has been commercialized for rapid prototyping of high strength thermosetting polymers and temperature resistant epoxies [10].

1.3 Fiber Reinforced Polymer Composite Additive Manufacturing

Efforts to combine the material benefits of composites with the cost and versatility benefits of additive manufacturing have been ongoing since at least 2001. Some of the first explorations combined short glass fibers with thermoplastics to enhance the strength and stiffness of FDM 3D printed parts [30]. Filaments were manufactured with set ratios of fiber to polymer which could then be fed into a standard 3D printer. Seeing immediate success, these ventures have continued to the modern day, even going so far to have become commercialized for enthusiasts and hobbyists. Two titans of 3D printing, MakerBot and Markforged, have both introduced short carbon fiber reinforced nylon filaments made for their specialty and multipurpose printers [31, 32]. Other well-known consumer brands have followed suit.

The printed composites have shown significant increases in strength and stiffness. Table 2 provides a list of several short fiber/polymer materials and their tensile strengths and moduli. Some retail options, like that of Markforged's Onyx and Kimya's ABS Carbon, show very little improvement over their matrix materials. Others, like MakerBot's Nylon Carbon Fiber and 3DXTECH's FibreX, show significant improvements. As has been explored by [33], fiber length and fiber content play a major role in the final properties of a printed part. Furthermore, there is a balance between toughness and fiber length, fiber content, and certain material properties. For example, toughness, ductility, and yield strength may decrease as fiber content increases, even though UTS and tensile modulus increase.

Table 2: Tensile Strengths and Moduli of Short Fiber FDM Composites

Material	Matrix/Reinforcement	Tensile Strength (MPa)	Tensile Modulus (GPa)
Markforged Onyx [32]	Nylon/Short Carbon Fiber	40	2.4
MakerBot N Carbon Fiber [31]	Nylon/Short Carbon Fiber	110	7.6
Kimya ABS Carbon [34]	ABS/Short Carbon Fiber	36.7	3.4
3DXTECH FibreX ABS+GF10 [35]	ABS/Short Glass Fibers	68	4.2

Explorations to improve the qualities of printed components included forays into both continuous fiber reinforced thermoplastic FDM and short fiber reinforced thermoset DIW. By using continuous fibers in FDM processes, the strength of the composite's reinforcement would vastly increase, although the matrix would remain at a lower

strength. On the other hand, short fibers in a high-strength thermoset polymer would vastly increase the strength of the matrix while leaving the reinforcement without improvement.

Continuous fiber FDM comes in two main forms. In the first, fiber is introduced into the thermoplastic within a modified print head as the printing process takes place, with a representative sample shown in Figure 1. Variations in the design have been tested, but they all feature a heating chamber in which a standard thermoplastic filament and a continuous reinforcing fiber are fed separately and exit together. Some will include pre-impregnation of the fiber with some form of epoxy or sizing [36, 37], while others use dry fibers [38-40]. The overall concept was explored as early as 2013, with some of the more significant developments in mainstream publications arriving after 2016. The material properties of a few research teams' work are listed in Table 3. With up to an eight times increase in tensile strength, the process has shown great promise for future implementation [41, 42].

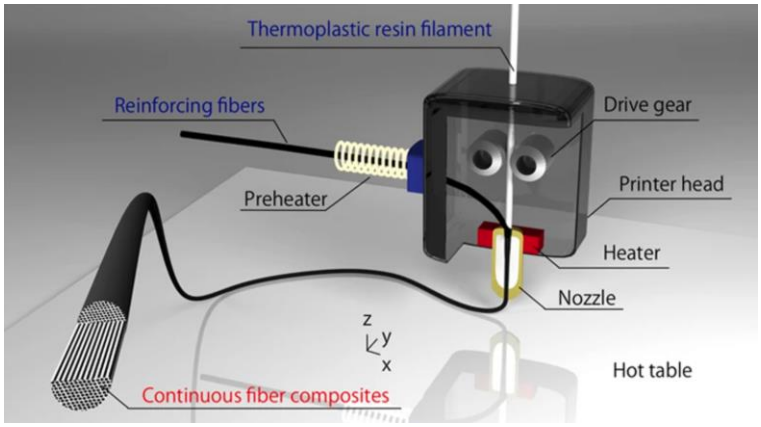

Figure 1: Continuous fiber FDM mechanism using a modified print head [38]

Table 3: Material and Mechanical Properties of Continuous Fiber/Thermoplastic Additively Manufactured Samples

Research Group	Matrix/Reinforcement	Reported Fiber Fraction	Tensile Strength (MPa)
Matsuzaki, et al. [38]	PLA/Continuous Carbon Fiber	6.6% by volume	225
Li, et al. [37]	PLA/Sized Continuous Carbon Fiber	34% by volume	91
Azarov, et al. [36]	PLA/Thermoset-Impregnated Continuous Carbon Fiber	18-25% by volume	511
Yang, et al. [43]	ABS/Continuous Carbon Fiber	10% by weight	147

In the second type of continuous fiber FDM, a filament of thermoplastic is manufactured with a continuous fiber inside, creating a continuous fiber and thermoplastic prepreg that can be printed on a normal FDM 3D printer [44]. This method has seen limited adoption and evaluation compared to the previously mentioned modified print head.

Like continuous fiber FDM, short fiber DIW has shown some promise in creating stronger 3D printed components, with one group reporting tensile strengths over 120 MPa [45]. In the simplest mechanism, an “ink” consisting of a thermoset epoxy base, rheological additive, and short fiber reinforcement is mixed and placed into a reservoir. The reservoir is pneumatically pressurized, forcing the ink through a nozzle onto the intended area of deposition. The rheology of the printing resin, length and direction of the short fibers, and printing direction have all been noted as major factors in the products of the process [10, 46-49].

While both short fiber DIW and continuous fiber FDM have shown potential to increase mechanical strength over short fiber FDM, neither has reached the lofty heights of strength achieved by woven or unidirectional composite laminates. The marriage of continuous fibers with high-strength thermosetting polymers remains uniquely capable of producing the strongest composites, and therefore has been pursued by a handful of research groups. Perhaps the greatest challenge faced by any potential printing mechanism is how extrusion is achieved. Unlike the filaments used in FDM, which can be fed into a print head with a compressive force, neither carbon fiber nor liquid epoxy have any means to be mechanically pushed through a nozzle and onto a print bed. Instead, either the fiber must be pulled through the print head, or the resin must be hydraulically or pneumatically pushed through the print head, carrying fiber with it.

In the earliest explorations of continuous fiber reinforced thermoset polymer additive manufacturing, the chosen extrusion mechanism was to pull the fiber through a nozzle using previously deposited fiber. In one case, this was used in conjunction with (likely motorized) roller wheel pairs that pulled fiber from a spool and reduced tension on it such that it could be easily pulled through the nozzle [50, 51]. The fiber was pre-impregnated with a thermal setting epoxy that became highly viscous at room temperature. Upon heating to a threshold below the cure temperature, the epoxy would significantly reduce viscosity and more easily mold and bond to previously deposited layers. Thus, a print head was created that would feed the filament prepreg, heat it, and allow it to be pulled out onto a printing bed. Once it was deposited, the epoxy would again cool and stiffen, allowing for more material to be drawn out after it. This process produced

parts with tensile strengths of 1476 MPa, a marked increase over other additive methods of fiber reinforced polymer manufacturing.

A similar process was pursued by another group. A fiber was pre-impregnated with UV curable resin, which was then mostly cured before being spooled for use in the printer [52]. The fiber was then fed through a nozzle, through a pressurized resin chamber, and out a final nozzle onto the print bed. The pressurized resin chamber coated the filament with more UV curable resin, which allowed the fiber to be cured and bonded to previous layers with UV lasers in-situ. However, the fiber was still pulled out the nozzle by previously deposited layers. Initial testing showed the cured samples had far lower tensile strengths in experimental testing than expected, reaching only 134.2 MPa.

Although both novel methods provided high-strength results and a clear pathway to print continuous fiber reinforced thermoset polymer composites, they lacked the freedom of design that FDM-based arrangements displayed. This is because fiber had to be pulled through the nozzle, and therefore could not be printed in an unsupported or partially supported manner without the possibility of pulling, flexing, and moving previously printed material. The system also tended to place high transverse stresses on the carbon fibers as they exited the printing nozzles, meaning fiber tearing during deposition was likely to occur.

To ameliorate the lack of printing freedom and avoid the damage to fibers inherent in extrusion methods that require fiber pulling, options that provided a pushing force to the fiber are in early stages of exploration. These are, broadly speaking, based on direct ink write technology, as a pressurized epoxy “ink” is being forcefully extruded. In 2021,

one such published work used a pneumatic cylinder to force a highly viscous epoxy through a cylindrical nozzle. A second, smaller diameter nozzle was nested within the main cylindrical nozzle, through which carbon fiber was fed into the flowing resin. The carbon fiber fed from a small spool located above the pressurized resin in its own, separately pressurized chamber. The pressure of the resin was balanced with the air pressure within the spool chamber to ensure resin could not flow up into the fiber chamber. Printed samples were made with thermally cured and UV cured resins. The thermally cured resins were highly viscous, such that their shape could be mostly retained after deposition. Tensile testing showed strengths over 195 MPa for unidirectional samples. The UV cured resins were also highly viscous, although their capacity for in-situ cure provided significant freedom in printing fully unsupported designs [53].

1.4 Previous Work: Novel CFDW Printing Process

In 2020, before the publishing of [53], early work was completed by graduate student Ryan Cowdrey on a similar novel printing process at the University of Oklahoma [54]. The printer and a closeup cutaway of its associated print head are shown in Figure 2. The print head contains a single pressure vessel composed of two main parts. At the top is a polycarbonate tube that contains a vertical spool of loosely wrapped carbon fiber. Below is a 3-cc syringe attached to the carbon fiber chamber with a gasket and collar. The syringe is filled with a UV curable resin and fitted with a metal Luer-lock dispensing needle. Carbon fiber from the spool in the upper chamber is fed down through the resin in the syringe and out the dispensing needle. A pressure regulator and solenoid valve provide air at a specific pressure to the print head. As the pressure is increased, resin is forced out through the needle. Viscous shear forces between the resin and fiber act to

draw fiber out with the resin, which is the system's extrusion mechanism. Because this is essentially a direct ink write mechanism with a continuous fiber added, the process was labeled "continuous-fiber direct-write," or CFDW. Once the resin-fiber system is deposited, it is rapidly cured by three, 5-volt 1.5-watt 405 nm unfocused lasers (stepped down to 3 volts to avoid burnout). The lasers are intended to be aimed onto the tip of the needle by turning a lead screw, which will raise and lower the pressure vessel of the print head (and therefore the needle) relative to the laser mount. The tip of the needle can be shaded using 3D printed collars that fit over the syringe, which ideally prevents any resin curing to the needle and clogging the system.

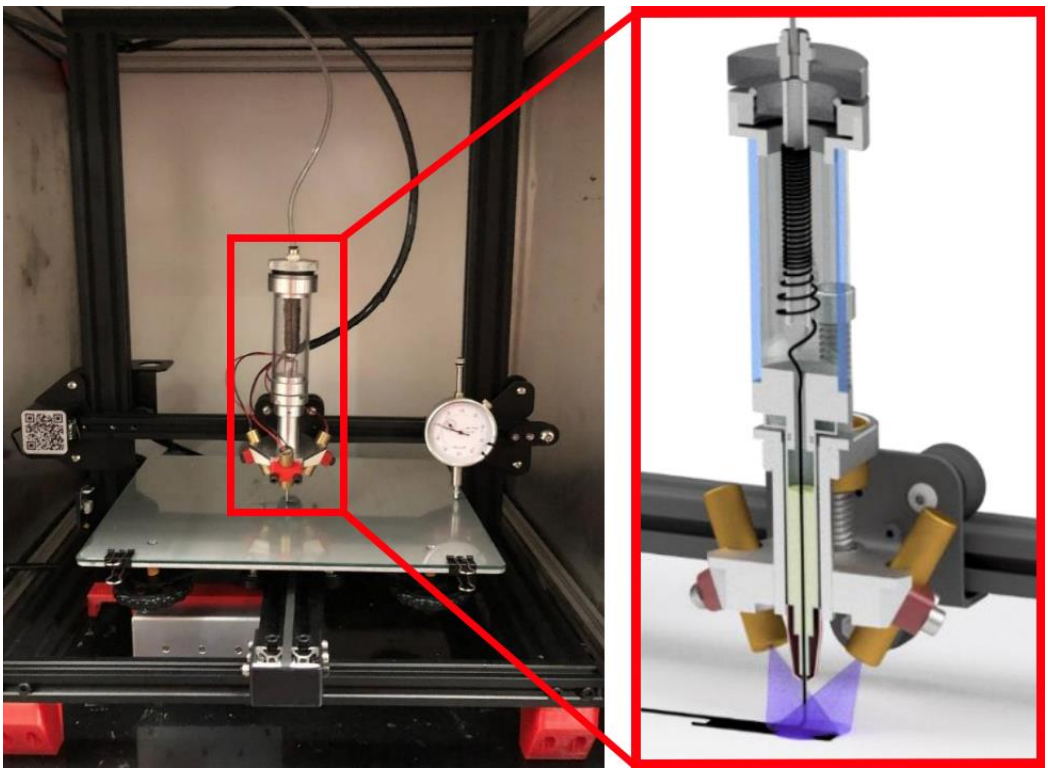

Figure 2: Initial CFDW printer and closeup of print head [54]

The primary focus of previous work with the CFDW printer was on tailoring printing parameters and proving its ability to print complex geometry. Feed rate,

extrusion pressure, and layer height were varied to provide samples that were quantitively and qualitatively examined to provide a set of optimal settings. Unsupported vertical and horizontal lines were printed to show that the rapid in-situ cure was adequate to allow for floating geometry. An airfoil and cone were printed to show that even complex unsupported structures were feasible.

1.5 Thesis Outline

This thesis is intended to discuss the evolution of the CFDW printer into its current state and provide a first look at the mechanical and material properties of its printed products. Chapter 2 will focus on early work, starting with the printer described in the previous section. It will include a re-evaluation of the original process, a discussion of several major design changes, and some of the printed products from this work. Chapter 3 will introduce the next full iteration of the printer with a description of the design, its motivations, and its performance. Chapter 4 will chronicle the testing and results of the printed products' material and mechanical properties. Chapter 5 will be a conclusion of this stage of the project and a look at possible future work.

Chapter 2: First Iteration Improvements to the CFDW Process

2.1 Printing Materials

Initial stages of printing were carried out with PR48 standard prototyping resin. This is the same UV curable resin used in previous work on the printer. It is notable in two regards. First, it has an open-source formulation that allows for modification and replication of work should it cease to be commercially produced. Secondly, it has a very low amount of photoinitiator compared to similar UV curable resins at only 0.4% Esstech TPO+ by weight. This means it requires far more light exposure, either in the form of density, power, or exposure time, to cure completely. The material properties of PR48 after a 10-minute post cure are given in Table 4.

Table 4: Material Properties of PR48 Resin [55]

Viscosity at 25 °C (cps)	400
Tensile Modulus (GPa)	1.4
Tensile Strength (MPa)	28
Strain at Failure (%)	3

Although previous work had been carried out with 3K carbon fiber tow, 1K carbon fiber was used in initial stages of the present work. This is because 3K tows were especially prone to shredding during deposition, which will be discussed in greater detail later. The fiber used was Toray T300 carbon fiber, with properties listed in Table 5.

Table 5: Material Properties of Toray T300 Carbon Fiber [56]

Tensile Modulus (GPa)	230
Tensile Strength (MPa)	3530
Strain at Failure (%)	1.5
Density (g/cm^3)	1.76
Sizing (% wt)	2.7

A rheological additive, Garamite 1958, was chosen to increase the viscosity of the PR48 resin. It is a proprietary substance composed of organically modified phyllosilicates [57]. It was chosen due to its low opacity when mixed, its relatively low necessary volume and weight concentration, and its high level of solubility within thermosets. It comes in the form of a fluffy white powder and is easily mixed using a Thinky centrifugal mixer. A 3-minute mixing cycle and a 3-minute degassing cycle provide for a visually homogeneous mixture with increased viscosity and slightly yellow tint.

2.2 Description of Original Printing Process

As had been done in previous work, the initial printing process involved a long list of steps before each print could begin. First, the vertical spool had to be removed from its pressure vessel by unscrewing the modified threaded cap to which it was attached. Carbon fiber would then be wound around the vertical spool by hand. The fiber would be fed down through the polycarbonate pressure tube, through the fiber pathway at the bottom, and out the bottom of the spool chamber. Two screws that held the syringe collar in place would then be removed and the fiber would be fed through a 3-cc syringe and out a metal dispensing needle. The needle would be locked onto the syringe, the syringe would be fitted onto its gasketed pedestal, and the fiber spool would be screwed back into the polycarbonate spool chamber. At this point, the syringe could be removed from its pedestal, filled with resin, and replaced. The syringe locking collar would then be fitted over the syringe and screwed down. The air hose would be connected to the top of the pressure vessel, and the whole unit would be pressed into the aluminum print head, where it would be held by gravity and friction between the syringe and the aluminum cylinder into which it fit. A small, 3D printed PLA shade would then be friction-fit onto the syringe.

The lights would be turned on by running a printing program that contained the command M106 S255. On a normal 3D printer running Marlin firmware, this command would turn on the cooling fan at full power. However, the modified CFDW printer used the board outputs to instead power the solenoid valve that turned pressure on and off and the three UV lasers. With the lasers on, the lead screw that adjusted the position of the syringe relative to the laser mounts could be raised or lowered until a shadow could be seen around the needle tip. The pressure regulator would be adjusted to the desired pressure, and the printer could then be restarted and given a printing program. The M106 S255 command would be run at the start of a print to start extrusion and turn on the lights, and the G-code path given in the rest of the program would guide the print head's motions. At the end of the print, the M107 or "fan off" G-code would turn off the lasers, close the solenoid valve, and stop the print. The printer would be turned off, the thread cut, and the printed part removed from the build plate.

2.3 Identification of Original Process Problems

Several process problems were observed during initial testing of the CFDW printer that led to what can be referred to as "failure modes." As used herein, a failure mode is a specific way in which the printing process breaks down, resulting in an inability to complete a print. These failure modes appeared due to a variety of reasons, and they were addressed roughly in the order they became problematic. The first of these that was encountered was the clogging of the needle tip. The UV curable resin would either immediately cure at the start of a print, or small crystals of cured resin would build up during the print until resin could no longer flow. This failure mode had a cascade effect in which, upon curing, the resin would bond the carbon fiber filament at its current

extruded length to the needle tip. The moving needle would then be pulled by previously deposited material, and the weak plastic syringe protruding out the bottom of the print head would flex accordingly. This would shift the position of the needle and light shade with respect to the lasers, causing the needle to end up outside the shaded area, in direct UV light. This would worsen the clog and ensure print failure if it occurred to a significant degree, but more frequently it was a subtle and gradual buildup of several full exposures that would lead to a failure. As such, the shade had to be moved closer to the needle tip to ensure that, even in a scenario where the needle was pulled, the light would not directly illuminate the needle tip. This had the drawback of reducing print fidelity. That is, sharp corners in the G-code path became large radii in the printed sample because the light was unable to solidify the deposited material in place until the needle was well out of the way. Previously extruded and unsolidified fiber would then be dragged by the needle until light caught and cured part of it to the print bed.

Once the problem of direct light exposure was partially addressed by moving the light shade lower, longer prints were indeed possible. However, it was observed that resin continued to cure prematurely and partially clog the needle over time.

The highest quality early print is shown in Figure 3. Although it shows some semblance to the intended G-code path, the lack of print fidelity is evident where the resin clearly extends far beyond the final positions of the carbon fibers. Furthermore, the surface finish is extremely wavy and, in some places, knurled by small crystals of prematurely cured resin.

Figure 3: Earliest successful printed sample (below) using unmodified printer with its intended G-code path (above)

2.4 First Modifications to the Original CFDW Printer

The best samples acquired in initial testing were deemed unsatisfactory, and the printer's reliability was pitifully low. So, attempts were made to ameliorate the causes of the observed failure modes. It was decided that the current print head, although intelligently designed to act as a heatsink and adjustable mount for the lasers, was too loosely constructed to consistently segregate the UV light from the needle tip. That is, the holder for the syringe was able to shift not only up and down relative to the lasers, but also left and right very small distances. It was therefore impossible to keep perfect alignment between the lasers and syringe needle during printing. Furthermore, the adjustability of the system was deemed unnecessary. There should be no need to raise or lower the needle tip relative to the lasers, assuming a small ring of shadow around the tip is always preferred and the lasers will always be mounted the same way. Finally, the

aluminum construction of the print head meant it lacked simple means of rapid iterations on its design.

So, a new print head was designed that would be manufactured out of PLA on a standard 3D printer. Its construction lent itself well to more time efficient iterative changes since new parts could be designed and manufactured in a matter of hours. The new print head (designated MkI) is shown in Figure 4. To address the problem of syringe bending, the syringe was now fully encased within a rigid PLA sheath. The sheath came in two halves so that, once the print head had been primed with fiber and resin, the fiber would not need to be threaded through the sheath's tip as well. The interior of the sheath was perfectly hollowed out for a syringe with a 0.5-inch, 18-gauge dispensing needle. This meant the needle and syringe were supported all the way to the tip. The sheath was also designed to shade the tip of the needle. Several sheaths were printed in succession with different outer diameters at the tip to tailor the shadow such that it would create a roughly 0.1-inch diameter ring around the needle tip. Lastly, the sheath had a set of three lugs on it so that, when the sheath was inserted into the laser mount and rotated, the sheath would not be able to move up, down, or come apart.

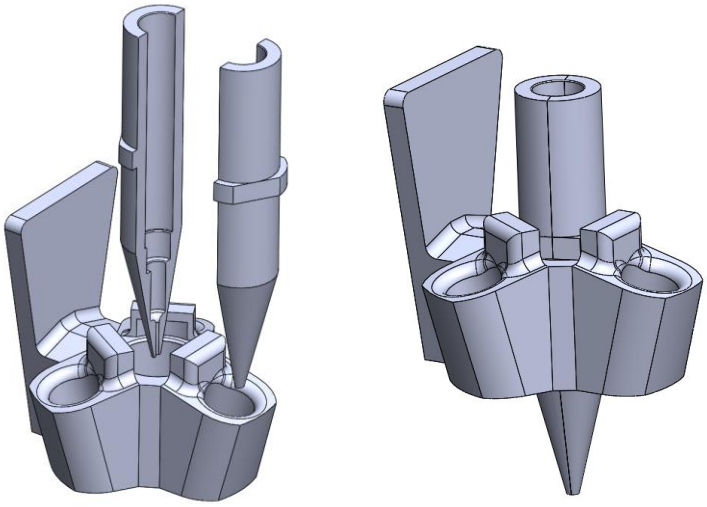

Figure 4: The new syringe holder and cover (MkI)

The new laser mount was attached to the printer's gantry using two screws that went through a flat backplate. The mount aligned the three lasers at a much steeper angle. This was meant to ensure that a generous, near cylindrical cone of shadow would extend down past the needle tip such that, if small inconsistencies were present in the vertical placement of the needle relative to the laser mounts, it would still be well shaded. It can also be said that, for the same ring of shadow cast at the bottom of the layer being printed, a steeper mounting angle would cure more resin more rapidly after exit from the needle. This is illustrated in Figure 5.

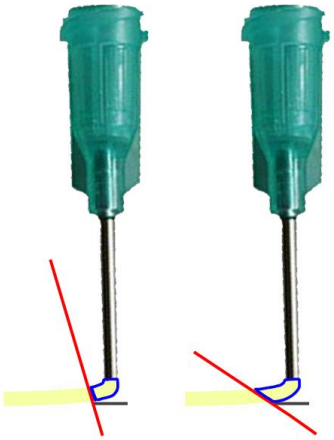

Figure 5: Illustration of laser mounting angle considerations with red lines indicating the leading edge of the UV light and uncured resin highlighted in blue

In testing, the new MkI print head showed promise in two ways. First, it succeeded in creating a shadow pattern around the needle and adequately stiffened the needle so that it was always shaded from direct light. One of the early shadow patterns is shown in Figure 6A, from which it was found that it was cast in a noncircular shape. This is partially due to one laser failing at the time. Test samples in the form of a square spiral, shown in Figure 6B and Figure 6C, were attempted several times, but the results were no more consistent than work with the previous print head. Globules of prematurely cured resin commonly became attached to the needle and the sheath that extended to the needle tip. These would then break off onto the print at random times and be cured to the surface. They were a very clear sign that the print head had not fully succeeded in preventing premature resin curing.

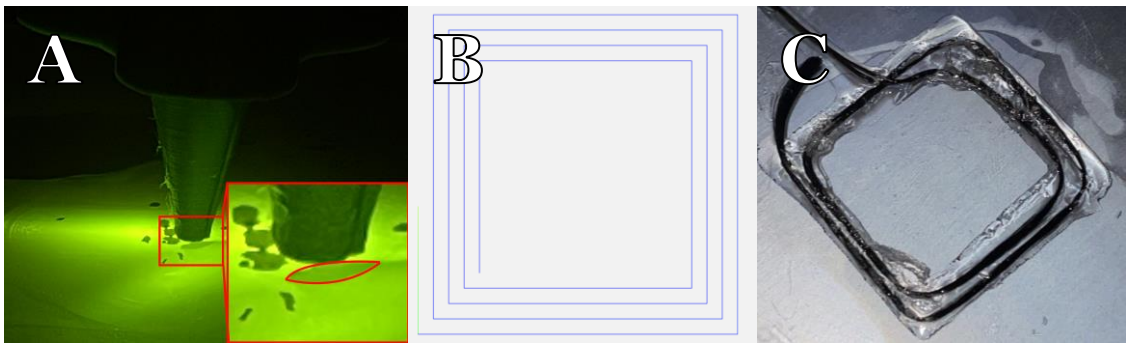

Figure 6: Print head MkI (a) shadow pattern, (b) intended sample path, and (c) printed sample

Because the MkI design had failed to produce consistent samples, a new MkII design was created that further simplified setup before printing and addressed some of the performance issues. It is shown in Figure 7. First, a dovetail plate was 3D printed out of PLA and attached to the 3D printer's gantry so that new print head designs could be easily designed, fabricated, and mounted to the printer. Next, a two-piece print head was created that featured a hinged design which made inserting the pressure vessel into the print head much easier. The syringe sheath was also made slightly shorter, allowing the needle to protrude by about 0.1 inches. This ensured no extruded material would become cured to the sheath and deposited later as crystals on the print's surface, as had happened before. Finally, the tip of the sheath was wrapped in aluminum tape to more completely isolate the needle tip from light by reducing bleed through the plastic. The resultant shadow pattern is shown in Figure 7C. It provides significant leeway around the needle and, once again, prevents direct light contact with the needle tip.

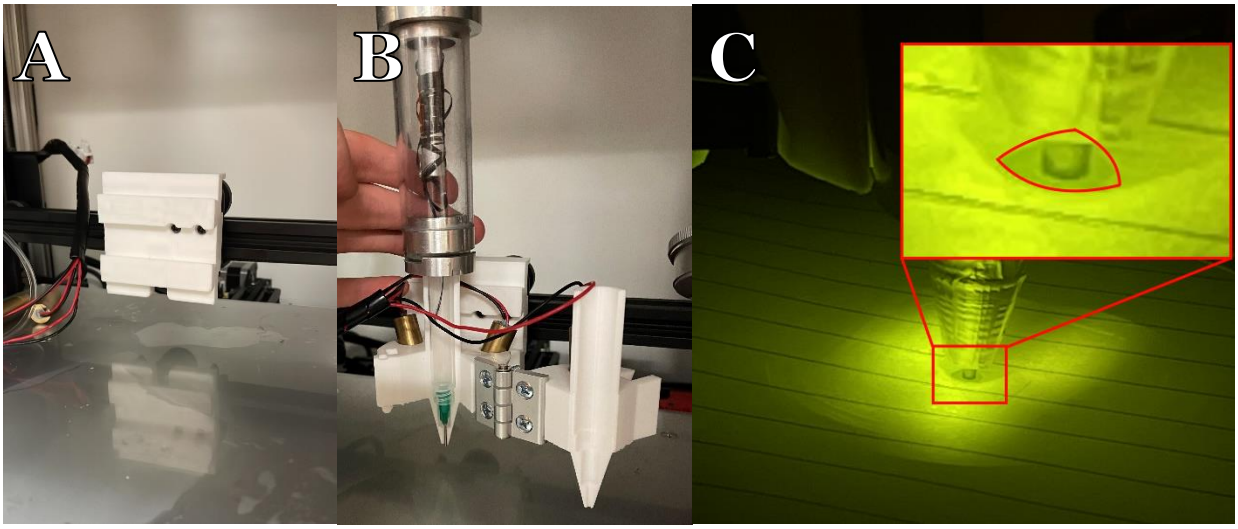

Figure 7: Print head MkII (a) dovetail mount, (b) assembled print head with hinge, and (c) shadow pattern

Regrettably, the MkII print head still did not solve the failure mode of needle clogging from premature resin curing. It was also not enough to prevent crystals forming on the needle tip and breaking off into prints. One such print is shown in Figure 8A. Over much experimentation, it was determined that the print bed, at that time a glass plate permanently epoxied on top of brushed aluminum, was reflecting so much light that resin was curing as soon as it was extruded. The voltage of the lights was immediately lowered to prevent this, but this was inadequate. So, the bed was heated until the epoxy weakened, and the glass print surface was carefully wedged off the aluminum plate. An absorptive black cotton fabric was laid between the glass print surface and the aluminum print bed, and the layers were clamped together with binder clips. A larger ring of shadow was also pursued by sticking layers of aluminum tape around the tip of the syringe sheath.

The combination of the rigid print head with an integrated shade and an absorptive print bed at last allowed for the completion of small prints with excellent surface finishes, as shown in Figure 8B.

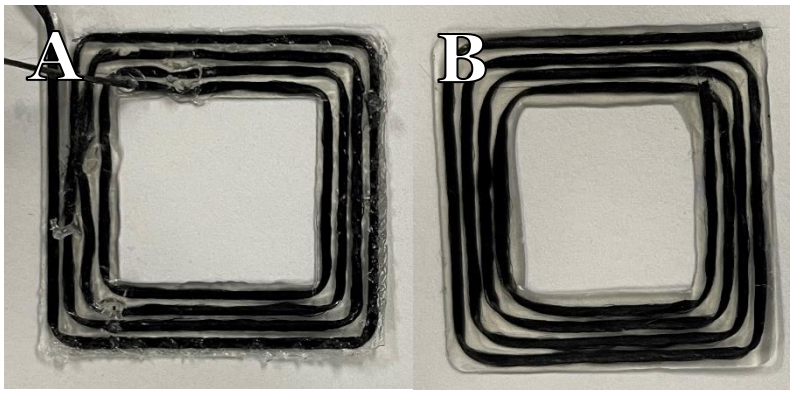

Figure 8: Print head MkII prints (a) before and (b) after adding light absorbing layer to print bed

2.5 Selection of Rheological Additive Concentration

It was at this point that the first complex geometry prints were attempted. One of the primary purposes of this printer concept is to enable rapid and easy fabrication of parts with high amounts of unsupported overhang. The tuning of this ability requires, among other things, a balance between the shadow size around the needle tip and the viscosity of the resin. If the shadow is smaller, the resin will have less time to flow before it is contacted by UV light and cured in place. If the viscosity is higher, the resin will take longer to flow, allowing for more time before it must be cured while still retaining the intended shape. The ideal combination would be an exceptionally high viscosity resin and a practically nonexistent shadow. There are, however, external influences on both values. The shadow must be large enough to prevent premature curing and needle clogging, even during small perturbations that move the needle. Furthermore, the resin viscosity cannot be so high that it becomes stuck to the inside walls of the syringe. Resin outside immediate access of the needle simply cannot be extruded, and the CFDW process lacks a way to introduce plunger or follower to push resin down to the needle. At this stage in the process, the shadow was deemed to be the minimum required size to prevent curing on

the needle tip, as it had been carefully developed over several iterations of needle shades. Therefore, the resin viscosity would be tested next. Several batches of PR48 resin were mixed using concentrations of Garamite from 0.5% to 9% by weight. It was found that concentrations below 3% flowed far too much to retain the intended shape, even when the resin was being directly extruded on the flat print bed. At and above 5%, the resin was so viscous that it would not flow down the syringe walls during printing, resulting in the printer running out of available resin mid-print. Since 3% and 5% existed at the threshold of functionality, they were included in a series of experiments in which cones were printed with resin that had 3%, 4%, and 5% Garamite concentrations. These cones are shown in Figure 9. The cones were all photographed from the side and the photographs identically scaled. Outlines were drawn around the cones to show their intended outer boundaries. Two conclusions were made from a visual comparison. The first is that a concentration of 4% Garamite provided the best fidelity to the original model. However, 3% Garamite provided the best surface finish, most likely because the resin could flow and form a smoother surface before curing. So, concentrations of 3% and 4% Garamite were chosen for future printing work, with 3% being used for prints that required good surface finishes, like tensile specimens, and 4% being used for more complex geometries.

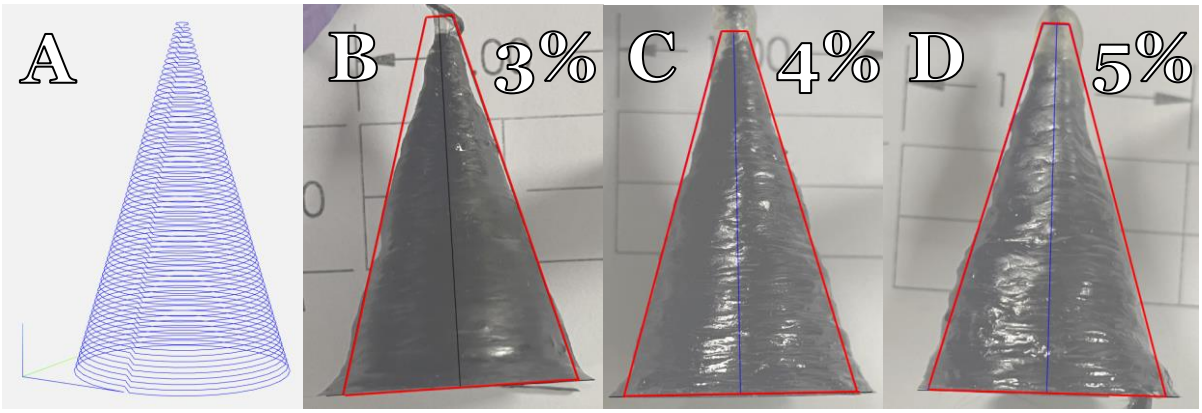

Figure 9: Cones printed to test varying concentrations of Garamite 1958 in PR48 resin with red lines indicating the intended outer profiles

Other influences of Garamite on printing were also noted during this work. First, an increased concentration of Garamite tended to slow the curing process. This meant that, even though less flow would occur before curing, the curing time would also be extended to some degree. This resulted in lower fidelity than expected, as shown in the 5% sample of Figure 9D. It may be because the resin opacity increased with increased amounts of Garamite, but it could also stem from some level of polymer chain-building obstruction taking place at the molecular level. Although this may be solved by increasing laser power or light density (by, for example, focusing the lasers), it was not deemed important to test since the printer currently lacks any way to reliably feed resin at such high viscosities, as previously noted.

2.6 Development and Use of IGES to G-code Translator Program

With the ideal resin viscosities identified, the intended next step was to generate a multi-layer G-code of a honeycomb pattern. Previous G-codes had been written by hand, but this would prove to be too inefficient for such a complex pattern. So, an over 800-line C++ program was designed to allow for more efficient G-code generation. The goal was to take a sketch made in SolidWorks and directly convert it into a G-code path. This would

make dimensioning and visualizing the path very simple. Next, the program would need to be able to stack this sketch an arbitrary number of times at an arbitrary layer height in a continuous manner. That is, the printer must never cease printing, and it must never have to reposition itself to continue printing, since the continuous fiber cannot be cut during a print.

The process of creating a G-code using the IGES to G-code program begins with a SolidWorks sketch. This must be a single sketch in a SolidWorks part file. Several restrictions exist on the location and orientation of the sketch in three-dimensional space, but the most straightforward use case of the program will be presented. A sample drawing is shown in Figure 10. It consists of two layers, drawn 10 mm apart for viewing ease, in a continuous string of lines. The bottom layer orients fibers primarily at 0°, and the upper layer orients fibers primarily at 90°, creating a small bidirectional layering.

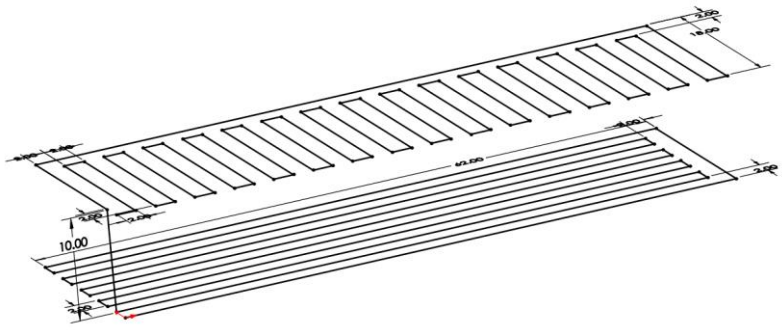

Figure 10: Perspective view of sample 2-layer bidirectional layup sketch in SolidWorks

Once the sketch is completed, it must be converted into a composite curve object. The file must then be exported as an IGES file type. This creates a plaintext file based on a rigid, open-source standard that can be easily parsed in C++ [58]. The program can then be run and pointed to the IGES file. A series of prompts will appear asking for the number

of duplicate layers of the sketch that should be created, the desired spacing between each layer, and the highest Z value in the original drawing. The IGES file will be opened, navigated, catalogued, and imported into vectors in the program, using the IGES standard to know where to look. The imported data will be further sorted into a list of coordinates, which are then inserted into a G-code template of "G01 X Y Z". If the operator chose to stack a drawing that was drawn in a single layer, the G-code will be copied, translated up the desired layer height, ordered in reverse, and added to the previous G-code for as many layers as were requested. Reversing the point order on alternating layers means that the final point of the previous layer will always be directly below the first point of the next layer, ensuring a continuous print path. If the operator input a drawing that had multiple layers, the G-code will simply be copied, translated up by the desired layer height, and stacked as many times as the operator requested. It is assumed that the operator would ensure the first layer begins at the same X,Y location that the final layer ends. The final G-code path of the sample drawing in Figure 10 stacked 3 times, 5 mm apart is shown in Figure 11.

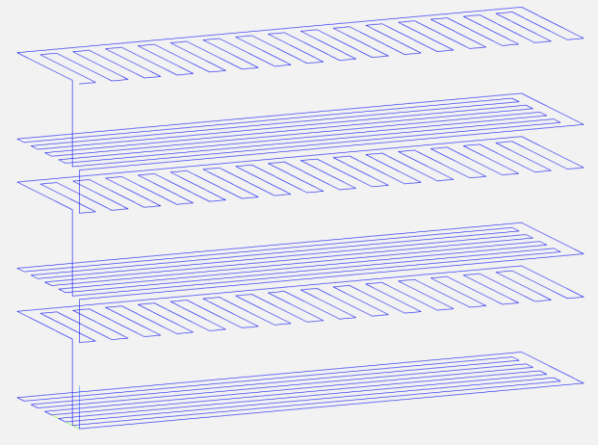

Figure 11: Final G-code path of the sample drawing after translation and stacking

2.7 Early Honeycomb Printing and Fiber Shredding Failure Mode

With a more efficient method of G-code generation available, a honeycomb sample was designed and tested. The intended shape is shown in Figure 12. It was stacked 20 times, with a 0.4-mm layer height.

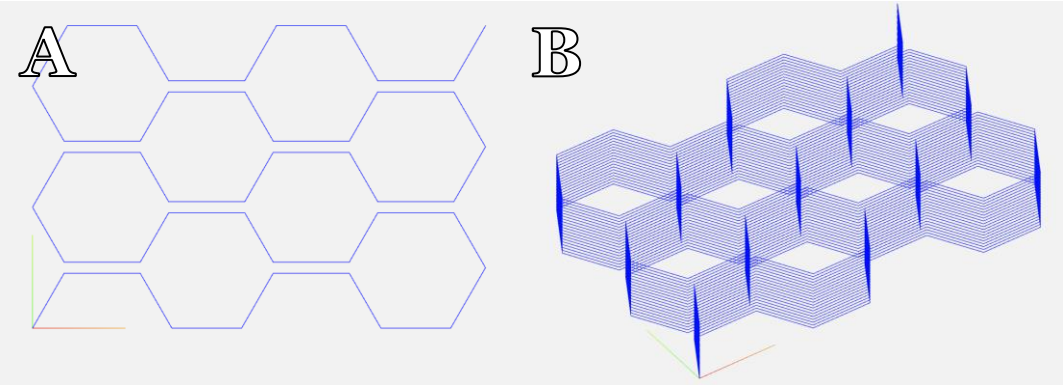

Figure 12: Honeycomb pattern G-code in (a) top-down and (b) perspective views

Figure 13 shows the early success of the honeycomb printing tests. The pattern was easily laid out on the print bed, and it was able to stack about 12 layers.

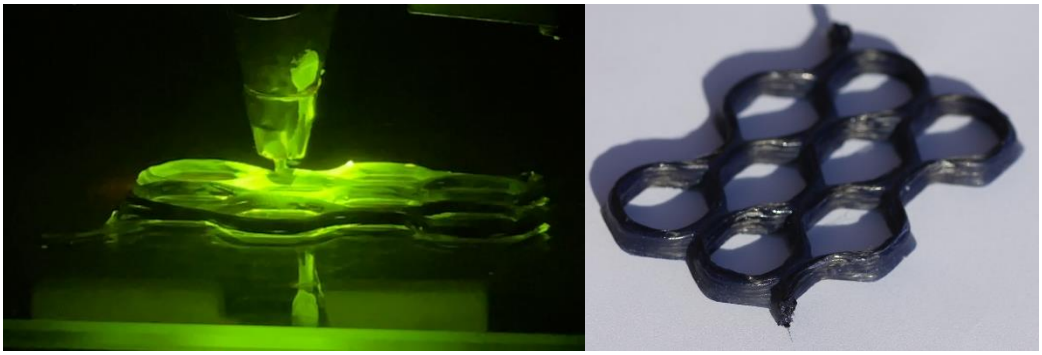

Figure 13: First honeycomb sample during and after printing

Unfortunately, the sample was not able to finish printing in the first few tests. It was at this point that a new failure mode was identified: fiber shredding. In very close observation of the printing process, it was noted that the fiber tended to exit the needle very close to the wall opposite the direction of movement. It would then be deposited very

near the top of the resin that was extruded. This resulted in a fiber shape during print as shown in Figure 14A. The fiber had to make a nearly 90° bend around the edge of the syringe. Over time, this would shred some portion of the 1000 fibers in the tow, and those fibers would stop moving in the needle. Eventually, as the remaining portion of the fiber would continue to be drawn through the syringe, that which had stopped moving would ball up within and above the needle until it was clogged. The result of this failure mode is shown in Figure 14B. It was especially exacerbated by prints that required long straight lines. Fiber shredding was also a major component of choosing a fiber tow size. Larger tows, like the 3K tow used in previous work, shredded far more rapidly than 1K tows for a given needle size.

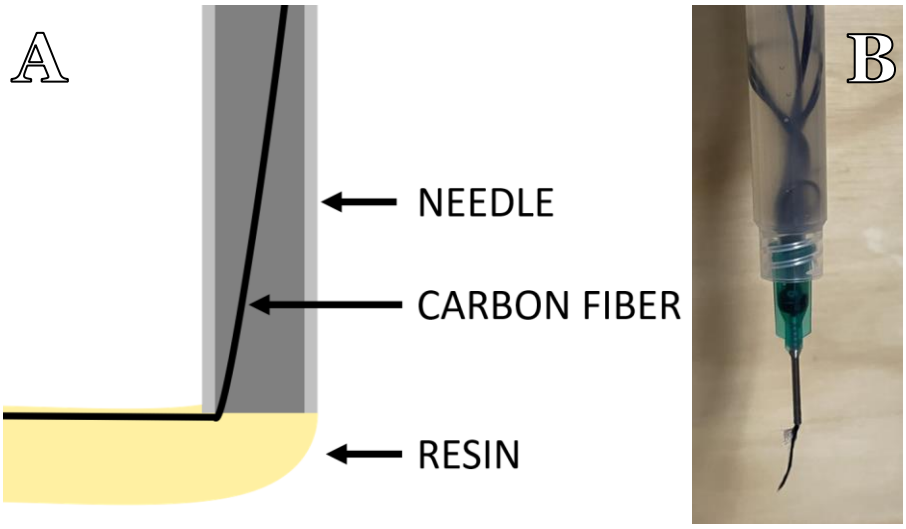

Figure 14: (a) Extrusion morphology showing nearly 90° bend in fiber and (b) image of fiber shredding failure mode

In an attempt to rectify this, a syringe with a needle was mounted in a lathe and spun. A carbide punch with a 45-degree taper was held in the lathe and pressed into the tip of the needle to flare the tip outward, like a trumpet's bell. The result of this modification is shown in Figure 15.

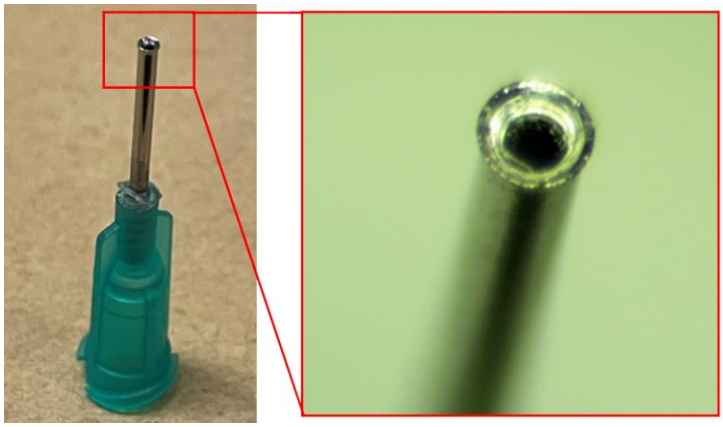

Figure 15: Picture with closeup of flared 18-gauge needle

With the new needles, the printer was able to produce long, multi-layer prints. An early, single-layer iteration of a tensile specimen is shown in Figure 16, where long lines of fiber were laid down without failure.

Figure 16: First successful specimen with long, straight lines printed using a flared needle

2.8 Prink Head MkIII

Work on a new print head began after it was proven that long prints could be accomplished without certain failure. This iteration was created to address two primary issues. First, the old print head featured a round light shade. It was noted that this did not produce a circular shadow, but rather a triangular one that meant the overall shadow area had to be larger for the minimum shaded radius around the needle to be about 0.05 inches. So, a new shade was designed by leveraging ray tracing in SolidWorks Visualize. The print head was imported as an assembly, and lights were fixed at the exact locations of the laser diodes. The shade was iteratively altered until a circular shadow was achieved. This work also allowed the shade to be moved further away from the needle tip, making

photography and observation far easier during printing. The new shade shape is shown in SolidWorks in Figure 17A and during a demonstration in Figure 17B. In practice, it provided the smallest possible shaded area while still keeping light a minimum distance away from the needle.

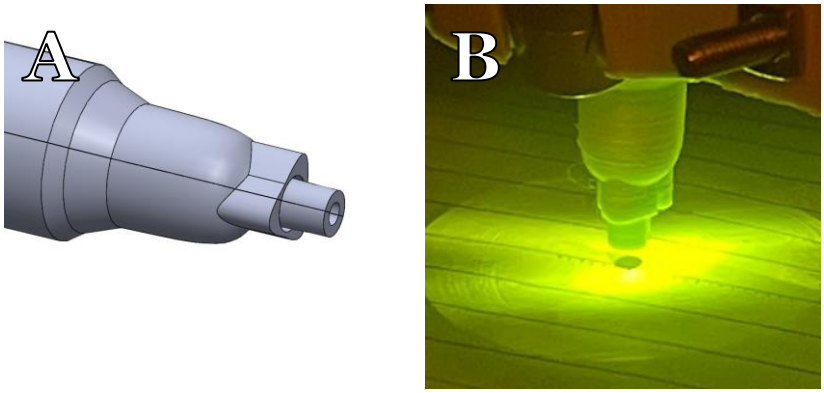

Figure 17: Print head MkIII light shade shape (a) in SolidWorks and (b) during demonstration

As a secondary goal, the new print head also more precisely held the lasers so that the center of their beams were focused exactly on the tip of the needle. This would provide the highest light density to the resin as soon as it was exposed to light, helping to better cure it in its intended position.

It was also considered desirable to be able to hot swap syringe shades, as iteration and repair would be faster if the shade were the only component necessary to remanufacture. So, a system of pegs was added to the shades with corresponding sockets on the laser mount, shown in Figure 18.

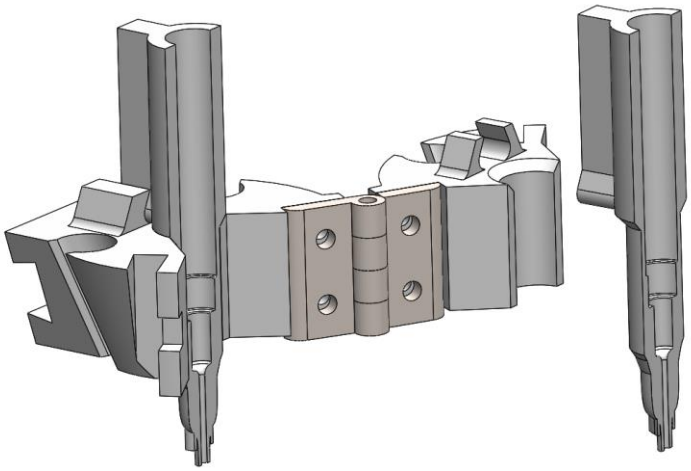

Figure 18: Print head MkIII with removable syringe sheath

2.9 Bed Adhesion Testing

The MkIII print head enabled some of the longest prints, producing several multi-layer tensile specimens. However, no complete specimens could be printed due to a newly identified failure mode. At varying times during printing, parts would begin to warp and pull away from the glass print bed until they became fully detached. Several changes were pursued to rectify this while printing resin without fiber in the shape of a tensile specimen. This eliminated the other fiber-related failure modes completely and allowed for rapid testing of bed adhesion solutions.

Other ongoing research within the SMIS lab using SLA photopolymers had shown that a resin's tendency to warp was dependent on the temperature of the resin during cure and the temperature difference between the resin and the build plate. In an elevated temperature environment, higher strength resins with long cure times would show a practically imperceivable amount of warping. After printing, a heated post cure in water would also keep the level of warping low. So, some of the first experiments to fix the lack of bed adhesion dealt with temperature manipulation during printing. In one case, the

glass bed was heated to 40° C in an oven, then immediately affixed to the printer and printed on. This resulted in the resin completely failing to bond to the print bed. Because heat appeared to worsen the issue, it was assumed that the print bed may benefit from being cooled significantly below room temperature. The print bed was therefore placed in a freezer and immediately printed upon. Like the heat, this only appeared to worsen the bed adhesion, although it did allow resin to bond in the early moments of printing.

With extreme heating and cooling ruled out, new hypotheses were constructed. It was possible that over time, the deposited material and glass print bed may heat up significantly as they were continuously bathed in UV light, causing the cured part to pull away from the print bed in a less extreme manner than when the print bed was intentionally heated. So, a set of stilts were fabricated that would raise the glass print bed away from the black, energy absorbing and thermally insulating fabric layer, and a fan was installed below the printing site as shown in Figure 19. This would ensure the minimum amount of heat was retained by the glass print bed while no extra disturbances were imparted upon the deposited material. However, printing with the raised print bed still failed to provide adequate bed adhesion.

With thermal issues unlikely to be the cause of warping and material delamination from the print bed, a bed surface priming approach was tested. A thin layer of water-soluble glue was applied to the glass bed using a standard Elmer's brand glue stick. This was then tested in three scenarios: one included an additional thin layer of PR48 resin, one included a thin layer of cyanoacrylate glue, and one was left without any additional priming. Of the three, the one with pure Elmer's glue performed the best, but it still did

not adhere the fiber-less print to the end of printing. The warp in the cured resin was still too significant and caused the edges to curl off the bed.

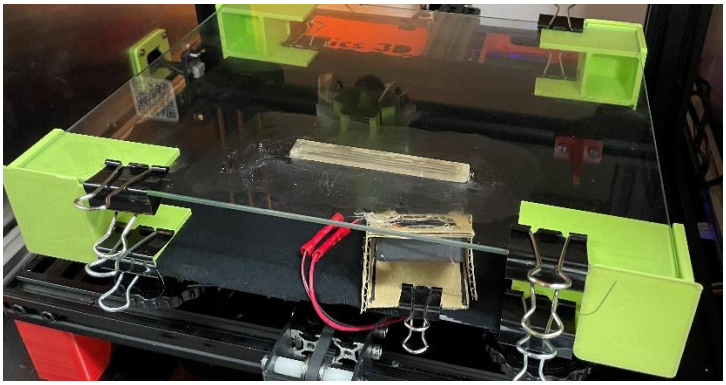

Figure 19: Raised print bed with priming layer of glue and cooling fan

Two more additions to the printing process were tested to reduce warping. The first included adding carbon black nanoparticles at a mass concentration of less than 0.01% to the resin. The resultant color change is shown in Figure 20. This would decrease the resin's rapidity of cure by decreasing the degree to which light could penetrate the resin (like the previously tested increased amounts of Garamite). It would also increase the opacity of cured resin so that, as resin layers built up, the lower-most layers would experience a lower degree of repetitive cure up to the end of printing, reducing the amount of part warping overall.

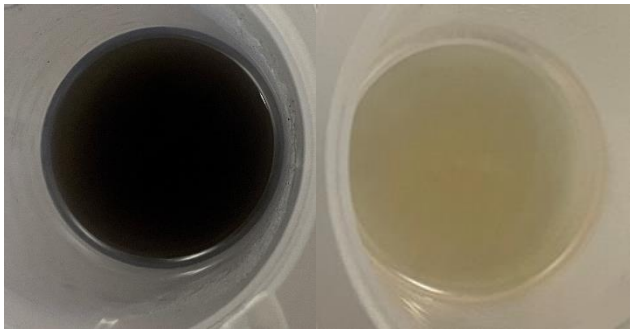

Figure 20: PR48 resin with 3% Garamite and less than 0.01% carbon black (left) alongside standard PR48 with 3% Garamite

Simultaneous to the carbon black testing, the print head was modified with a set of hanging shades that would restrict UV light to a roughly 1-inch diameter around the needle. Like the carbon black, this was intended to limit the UV exposure of previously deposited material. It would also create a more predictable final cure time for any printed part, since every region would only be exposed for a small amount of time each time it was passed over. Before the shades, the entire print would be exposed to UV light at varying light densities for the entire duration of a print. The shades and the resulting light pattern are shown in Figure 21.

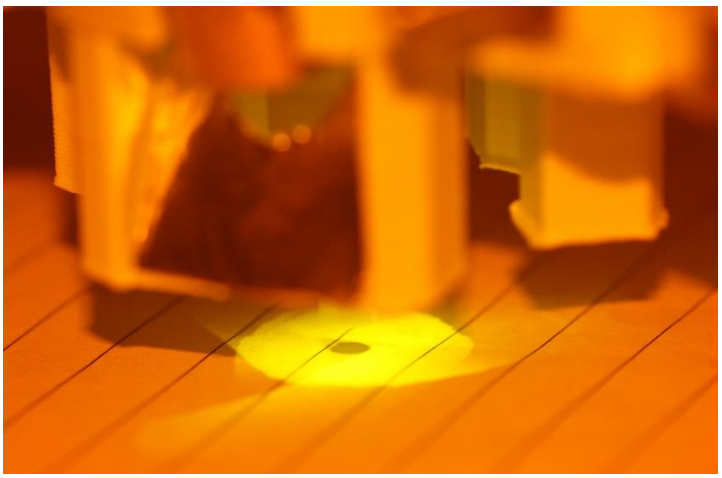

Figure 21: Hanging light shades and the resulting donut-shaped light pattern

More resin-only samples were printed with the raised print bed, fan, glue stick priming, carbon black, and hanging shades. These showed the lowest levels of warping and delamination yet. So, samples with carbon fiber were printed using the same configuration. The addition of reinforcing fibers served to significantly counteract the warping, so much so that no delamination was observed. Furthermore, it was exceptionally difficult to remove the parts from the print bed without damaging them, even using water to dissolve some of the glue. So, some changes were reversed. The carbon

black was removed from the printing process. It had the greatest negative effect on printing since it reduced print fidelity in the same way high concentrations of Garamite did. It would also complicate post cure for thick parts, since light would likely penetrate less material. The fan was also removed since prints were able to succeed without it. The hanging shades were kept because of their benefits for the predictability of cure times. Finally, the raised bed was kept to isolate the glass print surface from the light and heat absorbing fabric, since it was demonstrated that heating was bad for bed adhesion. With this, the failure mode related to bed adhesion was considered eliminated and the printer showed much higher rates of consistency and print success.

2.10 Print Parameter Testing

Over several months of printing, a system of determining optimal printing pressures and layer heights was developed based on the morphology of the resin-fiber system during extrusion. It is summarized in Figure 22. Figure 23 serves as a reference on relevant forces. TENSION 1 is the tension force required to pull fiber off its spool. VISCOUS is the viscous force enacted on the fiber by the resin flow. COMPRESSION is, practically speaking, enacted on the fiber by the print bed. FRICTION will occur between the corner of the needle and the fiber if the fiber is drawn taut. TENSION 2 is the tension enacted on the fiber by the previously extruded and cured fiber. It can serve to pull the fiber out of the needle if insufficient force is provided by the viscous resin.

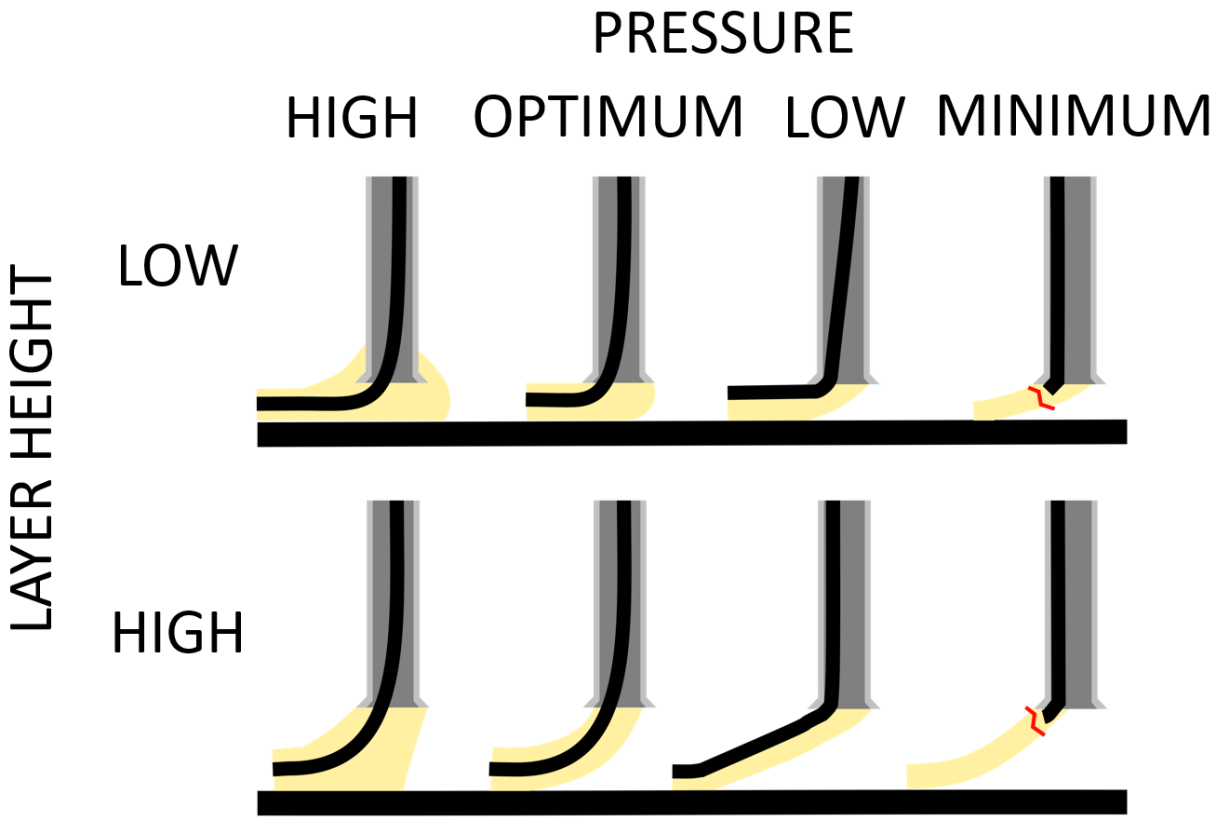

Figure 22: Relative pressures, layer heights, and their corresponding material flow characteristics

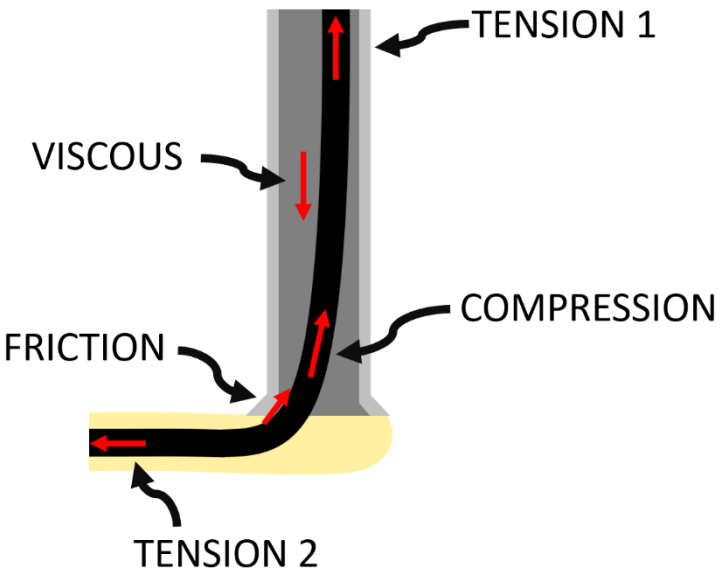

Figure 23: Simplified balance of forces on fiber undergoing extrusion

The system described in Figure 22 was generated with the primary focus of achieving a high fiber volume fraction while keeping printing failures at a minimum. The highest theoretical fiber volume fraction would come from the minimum amount of resin flow while still providing an extrusion force on the fiber. Resin flow is directly related to, among other things, the printing pressure. A higher pressure will lead to a higher resin flow rate. Therefore, the highest fiber volume fraction will occur at the lowest possible printing pressure. With clogging from prematurely cured resin nearly eliminated, fiber shredding was the only failure mode that had to be considered when selecting the printing pressure. Fiber shredding was most likely to occur when the fiber was most significantly stressed at the flared corner of the needle. Moving the fiber closer to the print bed would provide it with less vertical room to extend during its path around the corner. Therefore, a layer height high enough to give the fiber a wide bending radius had to be selected first. The minimum layer height is shown most clearly in Figure 22's "LOW-OPTIMUM" case. The layer height can also be higher, as shown in the "HIGH-OPTIMUM" entry. However, this will generally lower the predictability of deposited material and fidelity of the print. This is because the material will be momentarily suspended from the needle over its intended deposition site and therefore liable to being pulled and pushed around before curing to the layer below. So, such printing heights are not recommended except for extremely simple parts, like tensile specimens, which require very few sharp turns.

Next, the pressure of the resin needed to be raised to provide enough resin flow that the fiber was extruded, not pulled, out of the needle. Fiber pulling is shown in the "LOW" and "MINIMUM" columns of Figure 22—the fiber is taut around the corner of the needle because it is not being pushed out the needle with more force than it is being pulled

by previously deposited material. In Figure 23, pulling would mean that TENSION 2 is nonzero and equal to FRICTION and TENSION 1, while COMPRESSION and VISCOUS are negligible. On the other hand, if the pressure is too high, resin will begin to extrude out of the needle at a very high rate, encasing the needle tip and significantly reducing the fiber volume fraction. The low-optimum image shows a resin flow that does not exceed the boundary of the needle tip, but still provides enough viscous force to prevent the fiber from being pulled. In this case, VISCOUS is balanced with TENSION 1 and COMPRESSION, and TENSION 2 and FRICTION are negligible.

It should be noted that this system lacks any definitive recommendations on printing pressure or layer height. This is because small variations in resin viscosity require a wide range of pressures to print, and layer heights within a small range will be acceptable depending on the needle gauge, needle type, and fiber thickness. Perhaps the largest factor that adds to uncertainty is the tendency of Garamite to increase the viscosity of resin over time. The viscosity of freshly mixed PR48 and Garamite will be nearly identical across batches with the same concentrations. However, as time passes, the mixture will increase in viscosity. This means that, for a single batch of resin, the printing pressure used for the first print will be lower than the pressure used for the second print. This is most easily avoided by mixing fresh resin before each print. However, it is best for printing success that layer heights and printing pressures be visually determined at the beginning of printing, until more control measures can be added to the printer to ensure consistency in variables.

An additional variable to consider is printing speed. For a given resin viscosity, needle size and shape, and carbon fiber tow size, the optimal print speed is dependent on

print fidelity and the printer's ability to produce an optimal extrusion flow at the desired rate. Print fidelity will suffer under two extremes. A speed too high will mean that deposited material is not exposed to UV light for long enough to fully solidify. On the other hand, a speed too low will allow deposited resin to flow for too long before it is exposed to UV light and cured in place. This became the driving variable when determining the upper speed limit. A series of small, single layer rectangular prints were printed with feedrates of F30 to F210. For reference, in the Marlin firmware of the 3D printer being used, feedrate "F" codes translate to mm/min. It was found that speeds up to F150 showed very little visible variation in surface finish or print reliability. Next, to determine the print speed's effects on the printer's ability to handle complex shapes, a series of cones identical to those shown in Figure 9 were printed. It was found that F90 permitted the least resin flow while still allowing deposited material enough time in UV to cure to previous layers. Since cure time is largely independent of resin viscosity, needle size and shape, and carbon fiber tow size, the printing speed cap was set at F90.

Next, optimal extrusion flows will exist when the print pressure can be raised to provide a high enough viscous force such that the fiber is not pulled out of the needle by previously deposited material. This is most simply determined in testing. So, prints were run using a series of parallel lines to determine the maximum reliable speed (up to F90) for the various combinations of resin viscosity, needle size and shape, and carbon fiber tow size. One such test is shown in Figure 24. In every printing configuration tested so far, F90 produced acceptable results and reliability, and so was used consistently. Even prints without complex geometry were printed at the same rate as those with complex

geometry so that any characterization done on any printed material would be universally relevant.

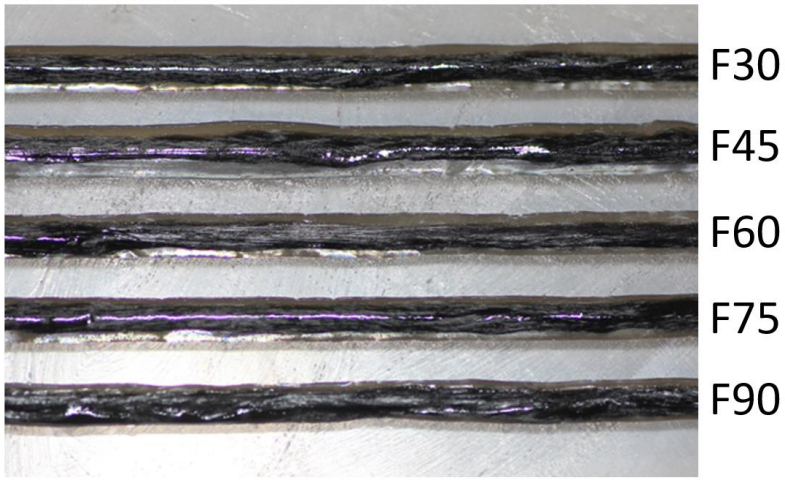

Figure 24: Print speed testing at speeds from 30 to 90 mm/min for a particular printing configuration

It is worth noting that the same correlation between high printing speeds and reduced printed line widths characterized in [54] was observed during the present work. This was not pursued as a means to increase the fiber volume fraction since the aforementioned influences on print speed determined whether a speed would allow the printer to function at all. Printing functionality took precedent over the properties of the printed material in all cases. Later work can make modifications from the current stable configuration to produce more favorable material characteristics.

2.11 Printing and Testing Procedure of First Material Characterization Samples

The printing consistency and reliability was deemed high enough to begin early material characterization work on test specimens. The specimens were designed to adhere to the ASTM D3039 standard for tensile testing of polymer matrix composite materials [59] insofar as the printing process would allow. The parts were printed in a long

rectangular spiral, shown in Figure 25, that kept the number of tight switchbacks low while still allowing for full unidirectional fiber alignment in the gage section. Since resin buildup is common at tight adjacent corners and can occasionally cause the needle to crash into printed material, the lines at the ends of the sample extend an extra 1.5 mm away before turning. This gives an overall length of 98.5 mm and a width of 12 mm. The samples were printed four layers high for a thickness of 2 mm. Printing was done with a flared 20-gauge needle, 1K carbon fiber tow, PR48 with 3% Garamite by mass, and at a printing speed of 90 mm/min.

Figure 25: Specimen printing path and final part as used in tension and burnoff testing

Tensile data was collected from five samples with masses between 2.1 and 2.5 grams using a 5 kN load cell on an Instron 5969 running at 1 mm/min. Before testing, the samples were given a 10-minute post cure in an Anycubic Wash & Cure machine. Three composite samples with masses between 1.7 and 2.5 grams were burned in a muffle furnace at 565 °C for four hours, in accordance with ASTM D3171-22 Procedure G [60]. Several samples of PR48 resin with 3% Garamite, neat carbon fiber, and neat Garamite were burned with the composite samples to verify that the chosen burnoff method did not have unexpected consequences. A sample of PR48 resin with 3% Garamite was cured in a silicone mold and measured in a gas pycnometer to find the density of the cured resin.

One fractured tensile sample and one whole sample were viewed under a Keyence VHX-7000 visible light ultramicroscope.

A honeycomb sample, using the same print path depicted in Figure 12, was also printed to observe the machine's current ability to create complex geometry.

Chapter 3: Further Printer Design Alterations

3.1 Resin Flow Inconsistencies, Spool Failure, and Capacity Restrictions of Previous Design

Although the printer showed significantly better reliability and consistency than before, areas of improvement remained. First, a change in carbon fiber vendors led to a change in fiber properties. The new thread had a more effective sizing that held fibers in a tighter bundle during printing. A lower amount of fiber dispersion within the resin in the needle appeared to uncouple the resin and fiber flow to some degree. That is, for small variations in fiber tension and position, the resin flow would change dramatically. At a given pressure and layer height, the extruded material would present as several of the modes of flow shown in Figure 22 over a short period of time, occasionally leading to fiber shredding or the needle being submerged in over extruded resin. Both would lead to a print failure.

A new set of print failure modes was also identified relating to two extremes in fiber behavior as it unwound from the vertical spool. In one case, the fiber would become caught on other fiber wrapped around the spool, vastly increasing the tension force on the fiber and momentarily pulling it taught. The dearth of fiber exiting the needle would cause an over extrusion of resin as the balance of forces and flow rates readjusted. At the other extreme, several loops of loosely wrapped fiber would simultaneously slip off the vertical spool. These would commonly orient themselves such that they would all be simultaneously drawn into the syringe. If they did not unwind, they would all be brought into the needle, clogging it, pulling the thread taught, and causing a catastrophic failure that put significant stress on the print head.

Finally, the current system lacked any way to print items that required more than about 50 feet of fiber or 3 mL of resin. It was noted in previous work [54] that extra resin could be added by pausing the print and refilling the syringe. This was impracticable since the print head had to be fully disassembled to access the reservoir. Not only did this seriously jeopardize print success by exposing the fiber to unavoidable tugging and accidental extrusion, it also would cause the printer to move its print head to the zero positions before continuing the intended path, destroying the print and crashing the print head in the process. On the other hand, the fiber limitation was due to the exponential increase in the previously described spool-related failure modes as the quantity of fiber increased. The reason for this can be explained with the help of Figure 26. When there is a high amount of fiber on the spool, as in the right spool representation, fiber pulled from a loop near the top of the spool must navigate around the bottom corner of the remaining fiber and quickly adjust to enter the small, straight hole at the bottom of the spool chamber. The bending required to do this commonly led to snagging and significant tension on the fiber. The resolution of the snag would either be the continued controlled unspooling of the fiber, or several loops near the bottom of the spool would come undone, leading to the clogs described previously. A lower amount of fiber reduced the chances of such things occurring, although it still did not fully prevent them.

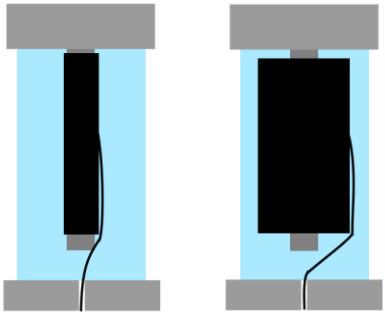

Figure 26: Vertical spools with (left) less fiber and (right) more fiber

Since a low amount of fiber was beneficial, the spool was rarely loaded with any more fiber than was necessary to complete a print. Unfortunately, this meant that any print failure would produce a leftover fiber too short for use. The fiber would have to be discarded, increasing material waste to an unsustainable degree.

3.2 New Spool Enclosure

A new spool enclosure and fiber dispensation process were developed to address the shortcomings of the previous design. First, to limit variations in fiber tension and ideally eliminate fiber tension entirely, fiber was placed on a motorized spool that unwound fiber slightly faster than it was being used. This ensured there was always loose fiber available to print. Secondly, to limit problems of fiber falling off the vertical spool and fiber quantity restrictions, a much larger horizontal spool with caps was fabricated. Lastly, the spool enclosure was removed from the print head, enabling future modifications that allow for the use of resin refill mechanisms and larger syringes. This also reduced the print head's weight, which helped with sagging.

The new pressure chamber that would contain the spool is shown in Figure 27. From left to right, the chamber has a CNC milled aluminum endpiece with a threaded hole and slot cut into it. The threaded hole accommodates a ¼-inch NPT to 5/32-inch

push-to-connect air hose fitting. The pressurized air enters the system here. The slot is cut to allow a 6-pin stepper motor cable through. After the cable was passed through, the slot was taped off and filled with two-part epoxy which cured to create a seal. The main body of the pressure chamber was formed by a 3.5-inch outer diameter polycarbonate tube with 1/8-inch walls. The tube is held to the aluminum end pieces with a two-part epoxy. A hole was drilled in the tube to fit a second ¼-inch NPT to 5/32-inch push-to-connect air hose fitting. A Teflon tube connected to this fitting bridges the spool enclosure and the print head to deliver the fiber with very low friction. An aluminum flange and cap assembly form the lid of the enclosure. A rubber O-ring is compressed between the flange and cap by tightening a set of three wingnuts, which seals the vessel.

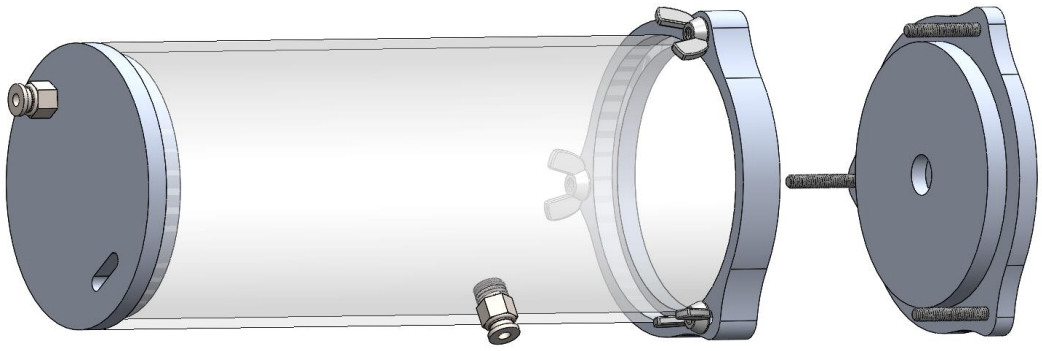

Figure 27: New spool enclosure pressure chamber

A toolless mounting bracket was 3D printed out of PLA that allowed the motor to be easily installed and removed without requiring the operator to insert their hand into the pressure chamber. The arrangement is shown in Figure 28. The cover (shown in blue) can be pressed over the motor until side latches lock in place and the motor is centered. A long screwdriver or rod can be used to unclip it, at which point the motor is free to remove. The walls of the bracket (shown in red) are centered on the endpiece using pegs

that align with holes that were CNC milled into the aluminum. The walls are held in place by a small amount of epoxy that can be easily broken should the parts need to be replaced.

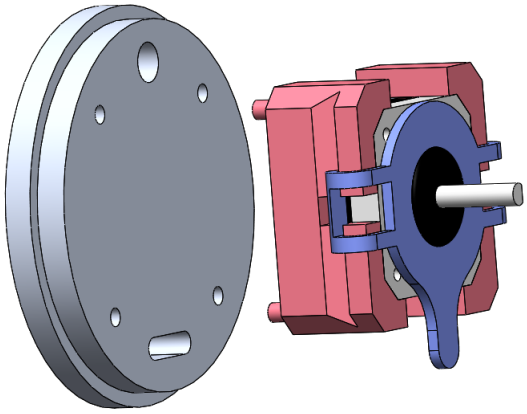

Figure 28: Motor mounting bracket within the new spool enclosure

A large 3D printed spool (Figure 29) spans the entire enclosure, connecting to the motor on one side and fitting into a milled circular pocket on the other. The spool has curved ridges at the left and right sides that discourage loose fiber from slipping over the spool walls, where it can become caught. The fully assembled spool enclosure is shown in Figure 30, where the blue 3D printed stands are also visible.

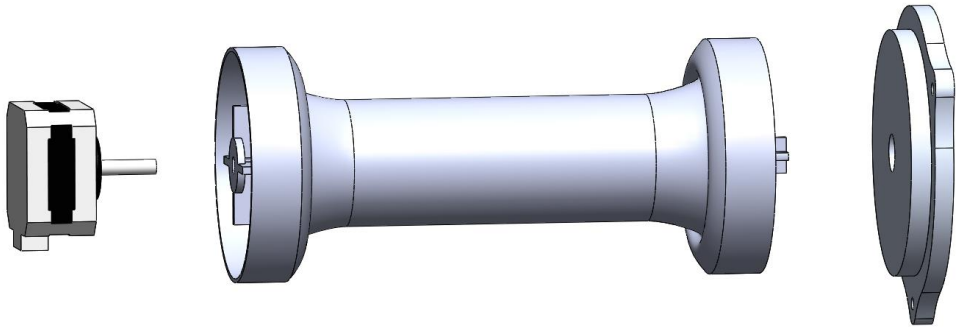

Figure 29: New spool designed to contain fiber without catching or tearing

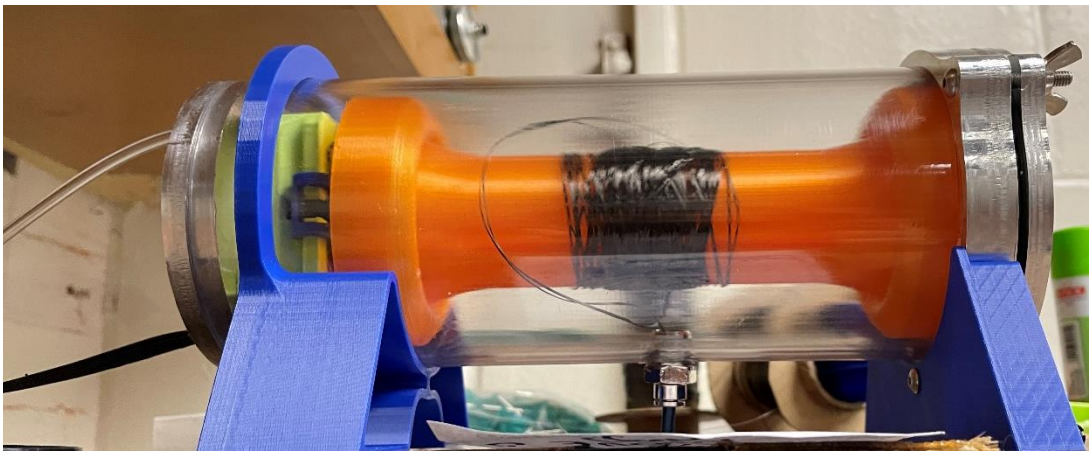

Figure 30: Completed new spool enclosure

As previously mentioned, the fiber is carried from the enclosure to the print head through a Teflon tube. The tube connects to the syringe via a pneumatic syringe cap modified with a push-to-connect fitting (Figure 31). The full printer in its latest configuration is shown in Figure 32.

Finally, the IGES to G-code translation program was altered so that it optionally adds an extrusion (or "E") code to the end of each line. The distance between each pair of consecutive points is calculated automatically, then added to the line. Then, in each G-code program that the printer runs, the code "M92 E24" is used to set the extrusion rate of the machine. Fiber is then automatically unspooled as the print head moves.

Figure 31: Pneumatic syringe cap with push-to-connect fitting

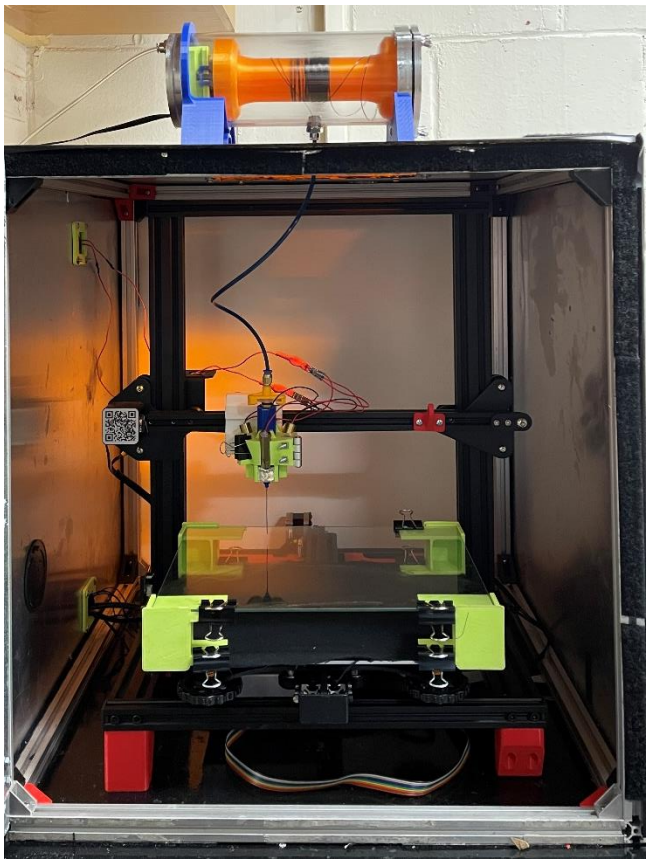

Figure 32: CFDW printer in its latest configuration

Printing with this new spool was more successful than ever before. Flow consistency stabilized significantly, and no spool-related fiber clogs have occurred since its implementation. The fiber length limitation was also successfully eliminated. Fiber is

loaded into the printer by using a specially designed key to attach the printed spool to a power drill. Full 100-foot tows are then rapidly transferred from their original cardboard spools onto the 3D printed spool. Fiber is fed down through the Teflon tube, then through the syringe as usual. Should any print failure occur, the fiber must only be cut and re-fed through the syringe, since significant excess is almost always present in the spool chamber.

3.3 New Needle Type to Address Fiber Shredding

A final modification to the printer was made in the latest stages of testing, as a new round of tensile and burnoff specimens were being manufactured. Despite all the reductions to fiber tension, fiber shredding still occurred on rare occasions. This is an unacceptable failure, especially as larger, more ambitious printing projects will be tested in the future. Although the flared needles had enabled printing so far, better solutions were sought to address the cause of the shredding more directly. Several needles were tested by threading fiber through them and pulling the same region of fiber back and forth over the edge of the needles at a 90-degree angle. Of the metal needles, all led to rapid fiber shredding and eventually total fiber breakage. On the other hand, plastic needles showed a practical inability to shred the fiber, even in the tested worst-case scenario. So, a tapered plastic 20-gauge dispensing needle like the one shown in Figure 33 was substituted in place of the flared metal needle.

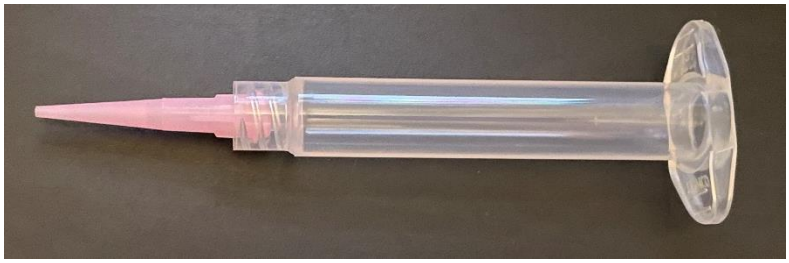

Figure 33: Newly adopted plastic 20-gauge needle

This option was originally ruled out because of the slight transparency of the plastic needles, but the syringe shading mechanism proved robust enough that resin curing inside of the needle has seemingly not occurred.

3.4 Printing and Testing Procedure of Final Material Characterization Samples

Identical tensile samples to those previously tested were manufactured with the latest configuration of the printer for a new round of tensile and burnoff work. This time, methods were used that were more applicable to unidirectional fiber reinforced polymer matrix composite materials.

Tensile testing was performed again with a 5 kN load cell on an Instron 5969 running at 1 mm/min, this time with 9 samples ranging in mass from 2.0 to 2.4 grams. Before testing, the samples were given a 10-minute post cure in an Anycubic Wash & Cure machine, then tabbed using fiberglass and Epon 862 epoxy. The epoxy was mixed with a 46:4:6 ratio of Epon 862 to Epikure Curing Agent 9553 to Epikure Curing Agent W. On each side of each end of the samples, two layers of fiberglass were layered with enough Epon to saturate the fiberglass. The epoxy was cured at room temperature for 48 hours, since heating to cure may have unintended effects on the composite samples. A tabbed specimen is shown in Figure 34.

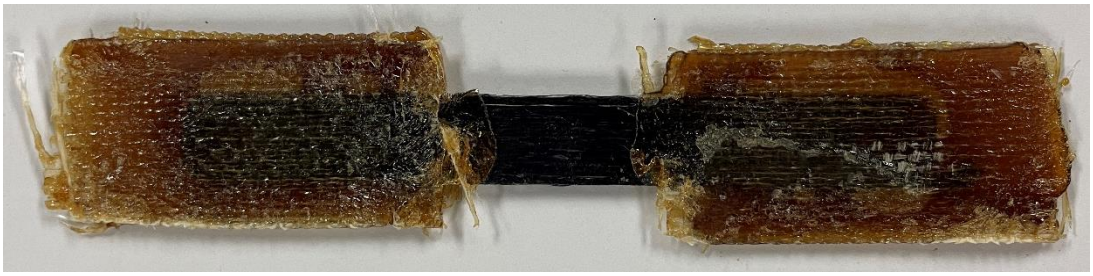

Figure 34: Tensile specimen tabbed with fiberglass and Epon 862

Three unbroken tensile samples with masses between 2.2 and 2.3 grams were burned in tube furnace at 600 °C for four hours under a sealed nitrogen atmosphere, in accordance with ASTM D3171-22 Procedure H. The nitrogen prevented any undesired oxidation or weight loss of the carbon fibers. Three samples of PR48 resin with 3% Garamite and 3 samples of neat carbon fiber were also burned under the same conditions.

One fractured sample was dried for several days in a wrap of paper to mitigate any unforeseen consequences of uncured resin being exposed to vacuum. It was coated with roughly 4 nm of iridium using an Emitech K575XD sputter coater. The sample was imaged using a scanning electron microscope.

Chapter 4: Material Testing Results

4.1 Tensile Testing Results

In the first set of tensile testing, no specimen broke outside the grip area. This resulted in a severe underperformance of the composites since stress concentrations determined the ultimate tensile strength. A graph of the tensile testing results is shown in Figure 35. The highest stress endured was 117 MPa, and the highest modulus was about 15 GPa.

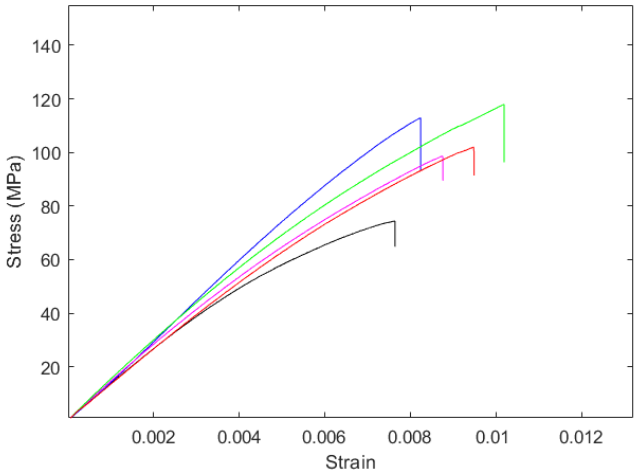

Figure 35: Uniaxial tension results from first set of tensile specimens

In the second set of tensile tests, the composite samples were tabbed with varying degrees of success. The final stress-strain plot is shown in Figure 36. The dashed lines represent tests that ended due to tab failure. The solid lines are tests that ended due to fracture. In the case of the solid blue line, the fracture was more progressive, with one major break being heard before the entire cross section separated. Others, like the solid green and black lines, saw an early dip in stress but continued until fracture. This is most likely a result of a small portion of the tab debonding, but enough stayed bonded to the sample that it was successfully fractured in the end.

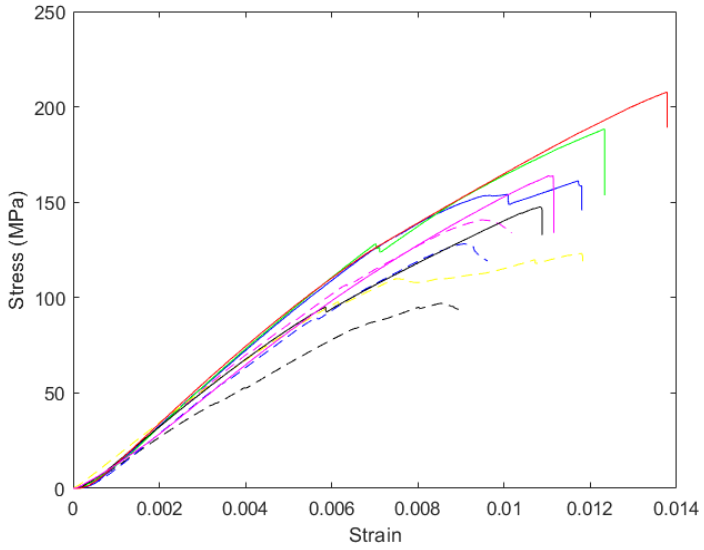

Figure 36: Uniaxial tension results from second set of tensile specimens with properly fractured specimens shown with solid lines

Of the samples that reached fracture, the highest saw an ultimate tensile strength of 209 MPa. The average modulus of the five fractured samples was 19.5 GPa.

4.2 Burnoff Testing Results

As in the case of the tensile testing, the first round of burnoff testing provided problematic results due to inadequate testing methodology. It was found that, in an aerobic environment, neat carbon fiber lost over 80% of its mass. This fully invalidated the first set of results.

In the second round of burnoffs in the nitrogen atmosphere, all fiber samples lost 2.5% of their mass. This corresponds well with the 2.7% by mass sizing applied to T300 fiber [56]. The neat resin samples carbonized with a consistent mass loss of 93.6%. These were acceptable numbers, so the results of the composite samples were also considered reliable. The densities of PR48 with 3% Garamite (1.143 g/cm^3) and T300 fiber (1.76

g/cm^3) were used with adjustments for carbonization stipulated by ASTM D3171-22 Procedure H [60] to find an average fiber volume fraction of 8.3%.

4.3 Microscopy Results

Ultramicroscope images of the surface of a tensile specimen are shown in Figure 37 and Figure 38. Several features are noteworthy in Figure 37. First, the fibers are very close to the surface of the part, as evidenced by the light reflections that highlight the curved resin around protruding fibers. Next, broken fibers—evidence of fiber shredding—are visible in various places and highlighted with red circles. Lastly, the surface of the resin is pock-marked. This could be because of very small air bubbles being present in the mixed resin, but it could also be the result of off gassing during the rapid curing process. It is also possible that they are not bubbles, but rather small crystals of cured resin, a theory supported by their non-spherical shapes. Figure 38 provides a quantification of the variations in surface height on a flat tensile specimen. Divots between fibers reach about 0.3 mm in depth.

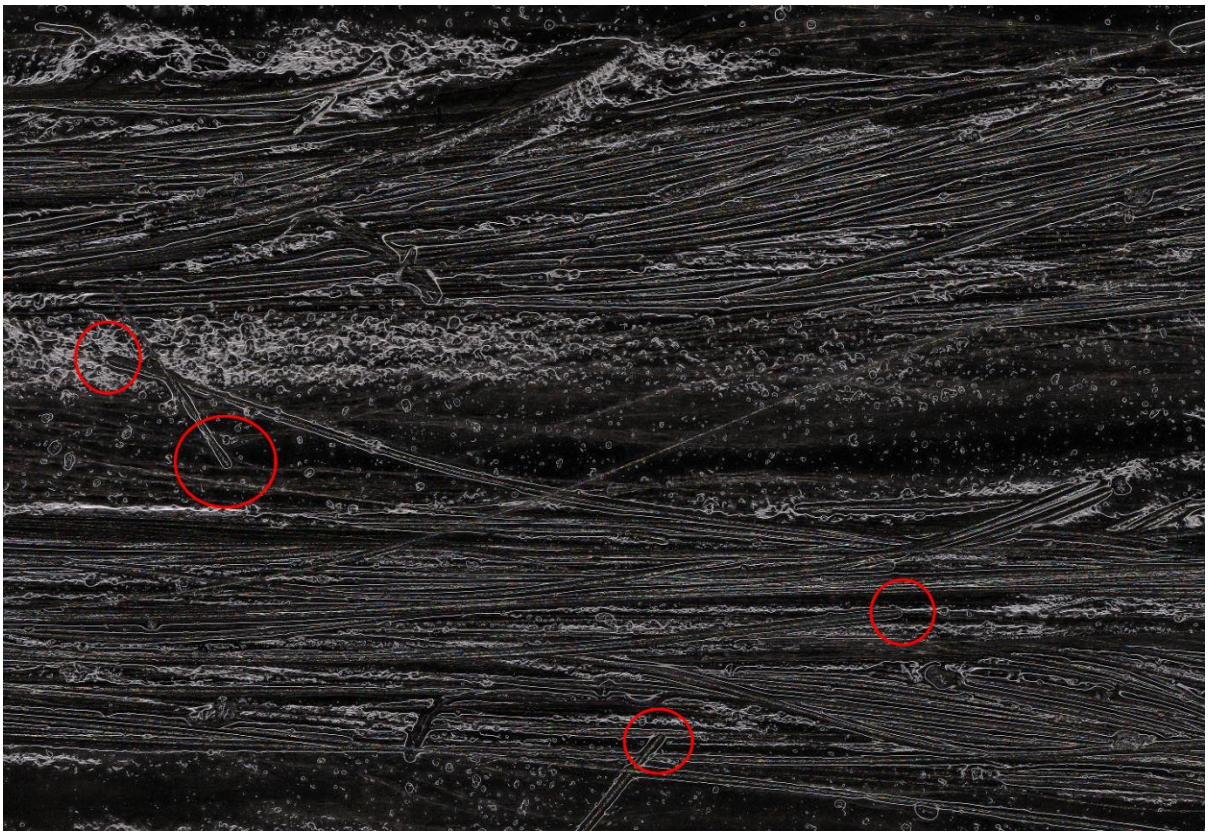

Figure 37: Ultramicroscopic image of unbroken tensile specimen surface

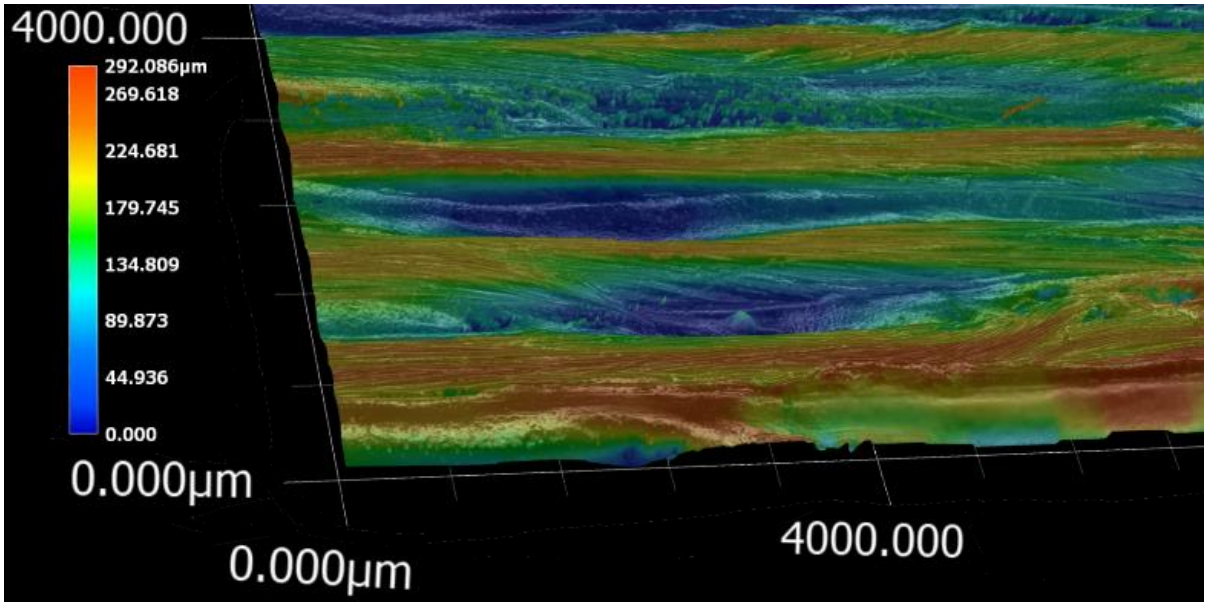

Figure 38: Surface depth analysis from ultramicroscope imaging

Figure 39A provides a glimpse at an exposed fiber bundle at the fracture site of a tensile specimen. This visible bundle is presumably from the core of a tow. Uncured resin is clearly visible pooling between parallel fibers, pointing to an inadequate degree of cure for resin shielded by outer layers of carbon in a tow. Figure 39B shows another perspective on the depth of an embedded fiber. It is well below the surface of the print, suggesting there is some variation in the amount of resin covering fibers depending on factors yet to be identified.

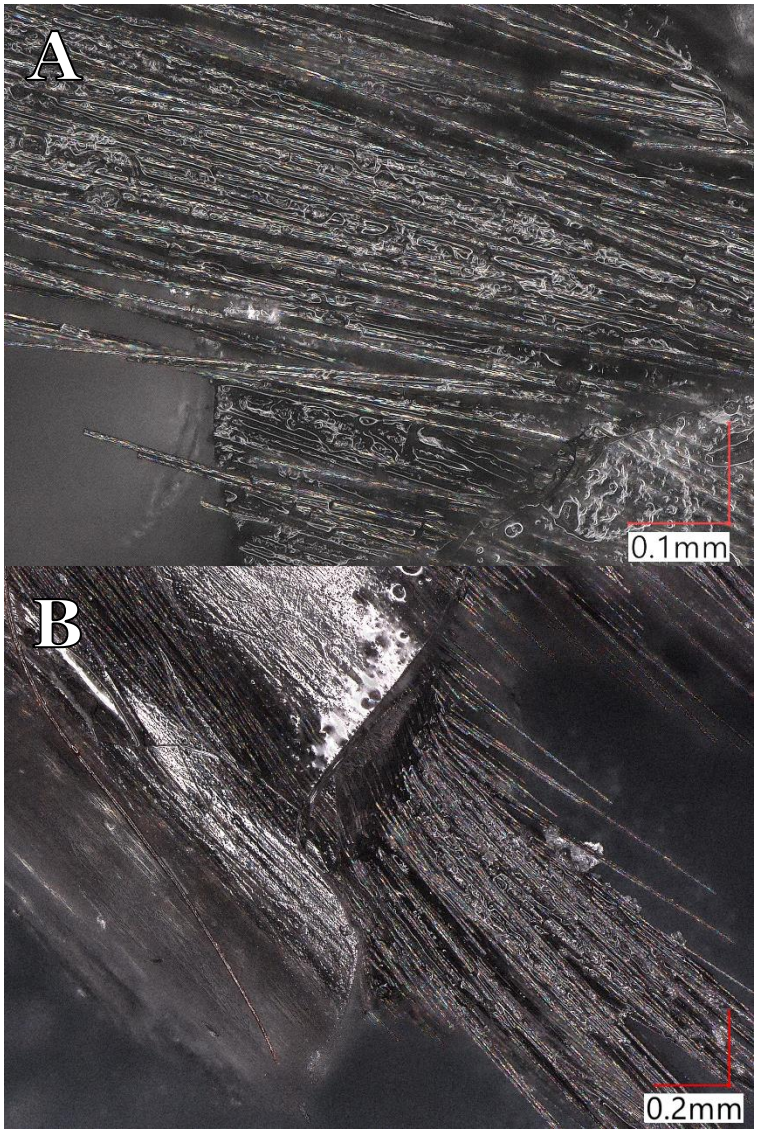

Figure 39: Ultramicroscopic imaging of fractured fibers showing (a) pooling of uncured resin and (b) the wider resin and fiber fracture pattern

Figure 40 provides a perspective view of the fractured sample imaged in a scanning electron microscope. Figure 41 focuses on a tow in the upper left of the cross section. First, a very large void exists in the center of the tow. This is an indicator of fiber pull out. Previous conclusions were made using the ultramicroscope that resin in the cores of tows may be uncured to a significant degree. It is therefore likely that the fiber that previously occupied this void saw very little resistance to pull out upon fracture. Figure 41 also shows

the surface of the composite part. A portion of each tow on the surface is exposed, with fibers clearly sitting atop the epoxy layer. Figure 42 serves to further characterize the sample's surface. First, two spherical voids are visible, implying there are some voids present, at least at the top of a part. Next, there are many small, irregularly shaped crystals of resin partially embedded in the surface. This means the pock marks shown in Figure 37 are likely a mixture of both, although far more crystals are present than voids.

Two images help to show the amount of resin impregnation between fibers. Figure 43 looks into the core of a tow, where impregnation would be most difficult. Resin is visible between the fibers where they exit the fracture surface, suggesting resin impregnation of the 1K tows is being accomplished during extrusion. Figure 44 shows the periphery of a tow. Dozens of cylindrical holes exist where individual fibers were torn out of the matrix during fracture. However, the fibers are well encased in resin. As the density of fibers increases toward the core of the tow (in the bottom right corner, in this case), a much larger cavity can be seen. This again could support that the resin and fibers shielded from the UV light do not fully cure together, leading to pull out of the tow's core. It could also suggest that that region of resin was simply better bonded to the many fibers it was between than to the surrounding matrix and was pulled out during fracture.

One important consideration in the CFDW process is that each tow and the matrix surrounding it is laid down individually. This could lead to delamination or interface-related failures where the matrix material from one deposited line contacts another. Figure 45 was taken between two parallel tows (one to the left and one to the right) to investigate if this was the case. In fact, the boundary between the two lines of material is entirely indistinguishable. This would suggest that the matrix layers are very well bonded

and see near isotropic material properties. Also of note in Figure 45 is the lack of voids. Even with extrusion and layering, the void content of the matrix within a part is very low.

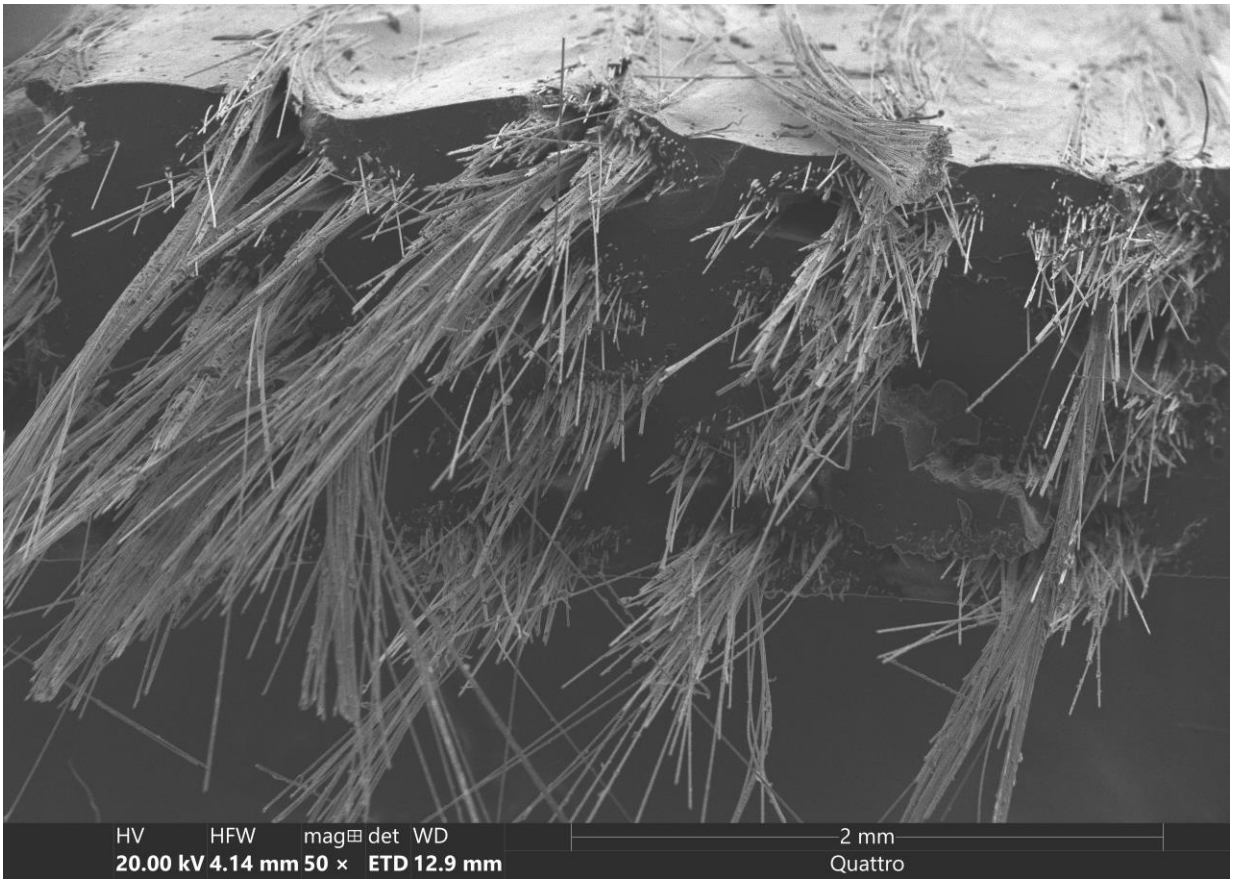

Figure 40: Perspective view of fractured sample imaged using SEM

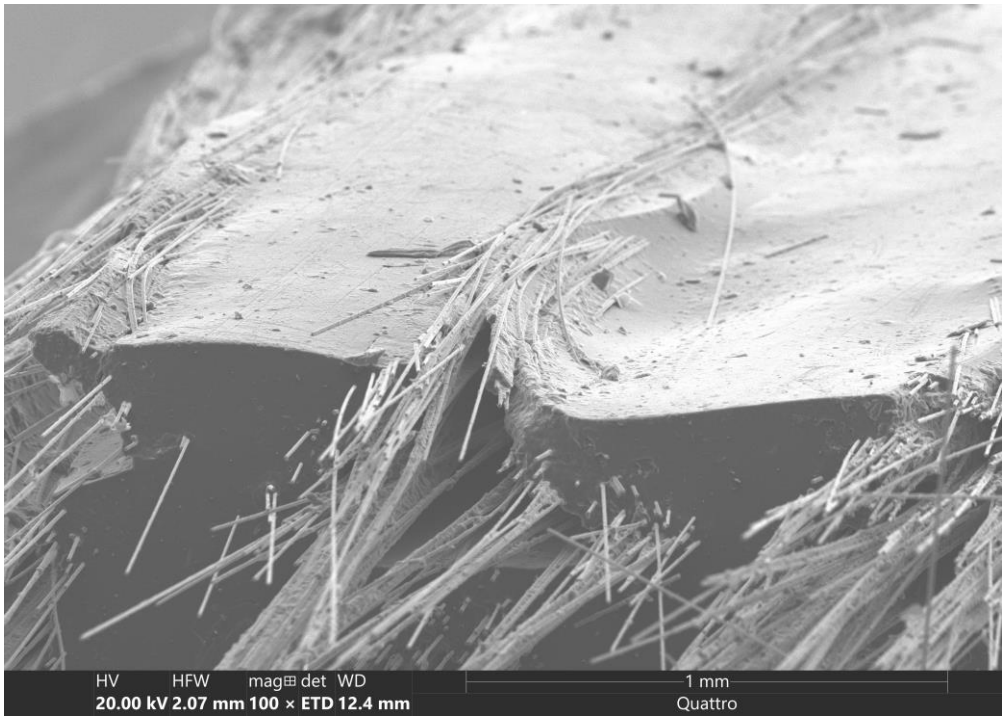

Figure 41: View of pulled-out fiber, surface roughness, fracture morphology, and exposed fibers on composite surface

Figure 42: Image of sample surface taken perpendicular to the part's surface well away from the fracture site showing two spherical voids and deposits of small resin crystals

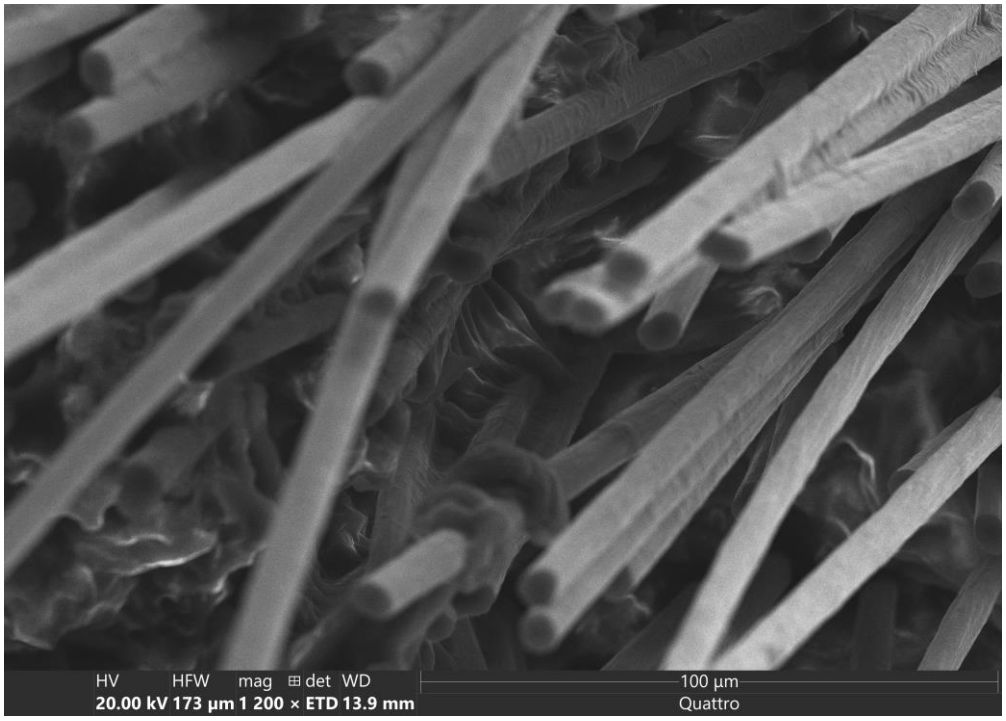

Figure 43: The core of a tow showing epoxy well-dispersed between fibers nearest the fracture surface

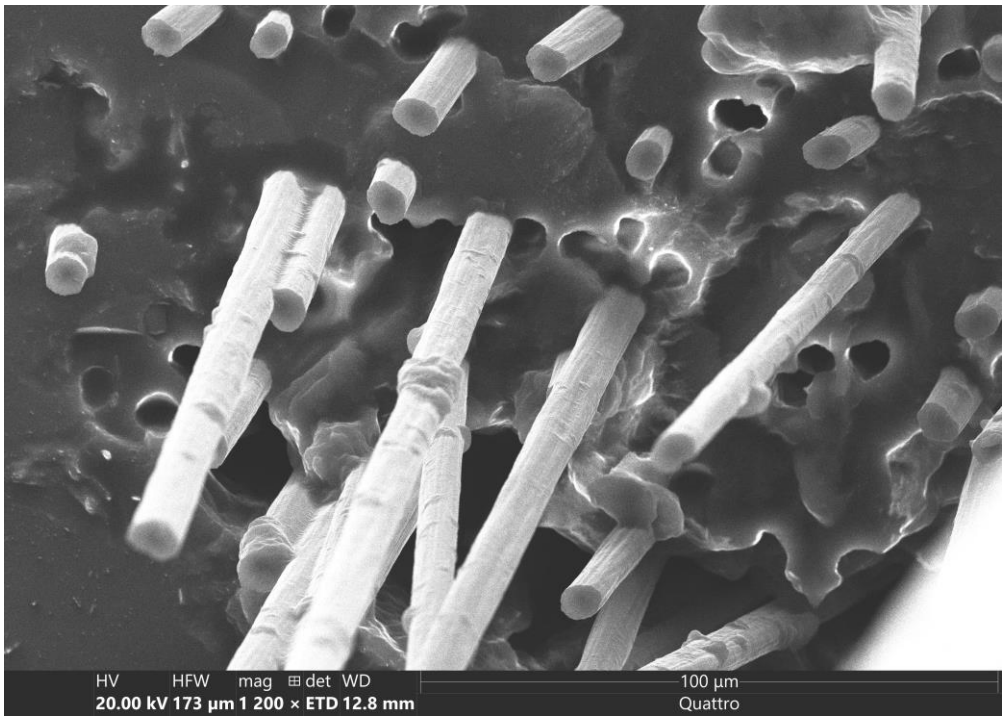

Figure 44: Fiber impregnation at the periphery of a tow and more evidence of pull out

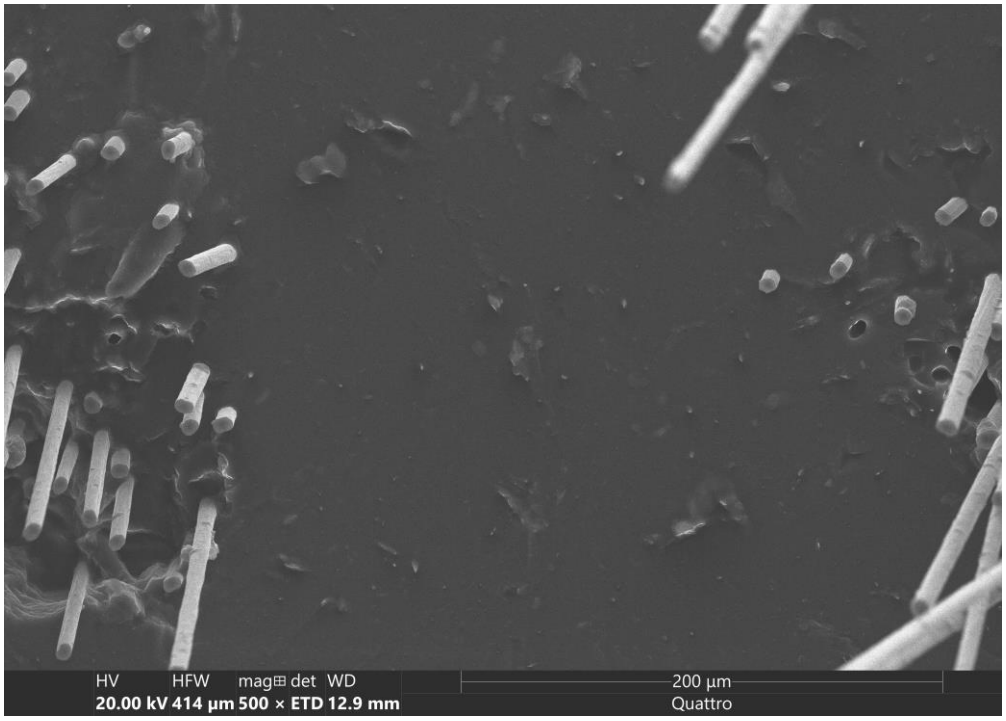

Figure 45: Matrix material on the fracture surface between two parallel tows showing no interface-related fracture geometry or voids

4.4 Complex Geometry Results

The honeycomb sample printed using the old vertical spool enclosure and latest print head is shown in Figure 46. In Figure 46B, the original G-code path is overlaid onto the printed part. Although the expected rounding of corners in present, the fidelity to the original G-code path is high, qualitatively speaking.

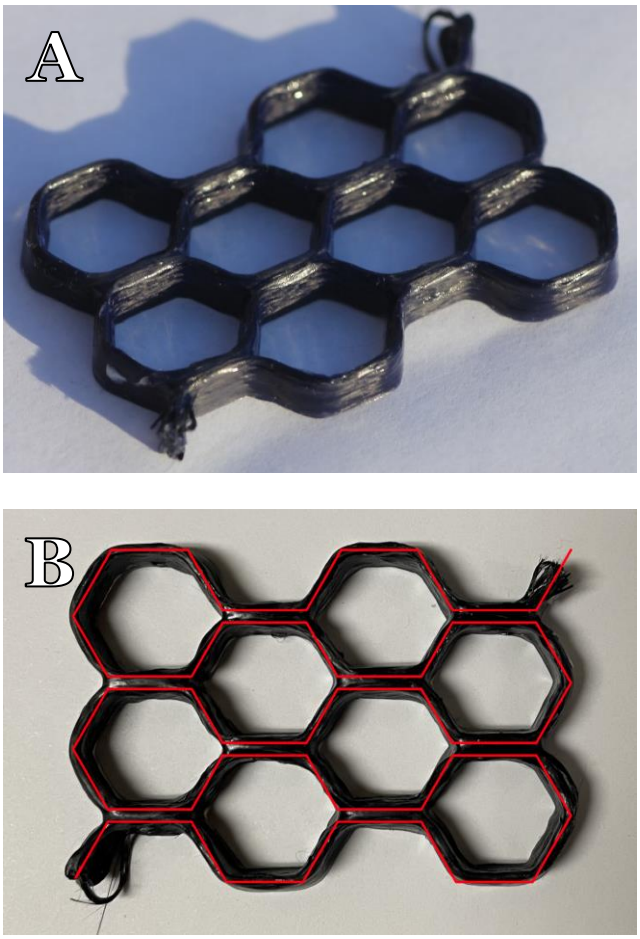

Figure 46: (a) Honeycomb sample printed with old spool enclosure and latest print head (b) with overlay of original G-code path

4.5 Sample Weight Consistency Results

An indirectly tested variable while printing dozens of identical samples was the range of masses one could expect for consecutive prints. It was found that prints of the tensile type used in other experiments were most likely to print with a mass between 2 and 2.4 grams using freshly mixed resin. As the resin batches aged and viscosities increased, masses as low as 1.6 grams were produced. This variability will likely be best controlled by mixing Garamite at various concentrations and directly measuring the increase in viscosity over time. Once maximum viscosities are identified, the

concentration used in an aged resin that has a viscosity most similar to freshly mixed 3% Garamite resin should be selected for future work. The resin should be mixed and allowed to congeal for as long as necessary to reach its maximum viscosity, then used in printing. This could potentially eliminate the necessity to vary printing pressure between batches of resin, meaning flow rates will be more consistent between prints.

Chapter 5: Conclusions and Future Work

5.1 Printer Design

Beginning with a prototype DIW continuous fiber 3D printer, a significantly more reliable platform was developed to produce early material characterization samples and support future testing. Failure modes in the CFDW process were identified and addressed. Needle clogging from premature resin curing on the tip was mitigated by using a light-absorbing fabric layer underneath the glass print bed and fabricating shape-optimized shades for the print head. Fiber shredding from spool-related fiber tension was solved by automatically dispensing fiber needed during printing. High transverse stress in extruded fiber at the needle's corner was lowered by migrating to plastic needles. Bed adhesion failures were solved with the application of a glue stick primer layer to the print bed. Finally, clogging caused by irregular fiber unwinding patterns was solved by switching to a horizontal spool.

With reliability significantly improved, the printer was further optimized for print consistency. The automated fiber dispensation contributed to a very low tension force on extruded fiber, keeping the balance of forces within the needle more constant. This, in turn, lowered variability in resin flow during printing. A set of hanging shades was added to the print head to create a more predictable curing time for parts. A method of optimizing the pressure and layer height was also developed based on observed flows and their potential for success.

Several efficiency and sustainability upgrades were also made, including a much larger spool that requires less time to prepare before printing and a hinged print head that makes the mounting of a syringe an easy task.

5.2 Material Properties and Characterization

A series of tensile and fiber volume fraction tests were carried out according to ASTM specifications on printed samples. The highest tensile strength achieved was 209 MPa, and the average tensile modulus was 19.5 GPa. The fiber volume fraction was found to be 8.3%. These values of fiber volume fraction, tensile strength, and tensile modulus are very competitive with other published values for continuous fiber DIW printed composites [53]. The fiber volume fraction was also acquired in a more rigorous manner than in [53], meaning it could be more competitive than it appears.

Several problems were identified in printed materials using ultramicroscopy. Fiber shredding, shallow fiber embedding, and, most significantly, uncured resin within fiber tows were all noted. These could all have serious effects on the strength and modulus of the material and should be pursued in further characterization and optimization work. SEM imaging further supported the theory that uncured resin exists within tows, as fiber pull out was identified in several places. However, it also showed the resin impregnation levels are high and bonding between individual matrix layers is excellent.

Finally, printed cone and honeycomb samples showed that the printer has potential for creating complex shapes.

5.3 Future Work

Future developments on the printer design could address several shortcomings of the current process. First, a new print head sized for a 10 mL syringe, potentially with a simple resin refill mechanism, could aid in increasing the theoretical limit on printed parts size. A new set of lasers could also be mounted to the print head with more shape-optimized shades that serve to cure material directly below the needle tip. This could

make unsupported printing more feasible, as extruded resin would be exposed to light even when under the shaded cone of the current laser arrangement. The current lasers could also be provided with a cooling method, either heatsinks and fans or liquid cooling, to prevent laser burnout and heating effects on the resin within the print head. A more direct addressing of the fiber shredding issue may also be possible by creating custom needles with rounded tips. If such needles were feasible, their internal flow channels could also be optimized to subject the fiber to varying pressures or flow directions, potentially aiding in resin impregnation should any deficiencies be found. Perhaps a fiber better distributed and encased in resin flow would result in less fiber shredding and resin flow inconsistency. It would also be in the best interest of the operator to acquire some control over the fiber dispensation (or extruder motor) speed during printing. As it stands, the fiber dispensation rate must be kept slightly higher than truly necessary to ensure there is always excess fiber ready to be extruded. This leads to loose loops of fiber within the spool chamber that, although not yet proven catastrophic, have the real potential to become snagged and cause print failures. Longer prints are more susceptible to this than shorter ones since the excess builds up over time. As a final augmentation option, linear rails could be added to the printer gantry. These are significantly more rigid than the current V-slot wheels and could aid in the reproducibility of certain shapes.

Further material work should also be undertaken to fully characterize the printer's products and capabilities. First, printing with 3K carbon fiber tow was proven possible and reliable after the alterations made to the printer during the present work. However, sufficient time did not exist to fully optimize the printing process and characterize printed products with 3K tow. In combination with custom needles to tailor flow and reduce

shredding, 3K (and higher thread count) fibers could unlock very high fiber volume fractions and part strength. All carbon fiber products should also be closely examined to understand the extent of resin cure within the fiber bundles. If it is found that resin is failing to cure, modifications to the current platform like increasing laser output power could help to ameliorate this. If such solutions are not successful, perhaps lighter colored and translucent materials like aramids and fiberglass would be more well-suited to the CFDW process with in-situ curing. The development of a resin with both UV- and thermal-cure mechanisms could also help to solve the lack of resin cure within carbon fiber, as a short, heated post cure could be added after printing to ensure full cure. Three-point bending tests would also contribute to an understanding of the produced materials, especially as fiber orientation and organization is varied within the print.

The CFDW process also lends itself well to explorations of new technology. The many types and applications of multi-material DIW additive manufacturing are especially relevant [61]. Multi-material DIW processes could be used to strategically inject strain sensing particles into the material as it is layered. Nanomaterials, such as carbon nanotubes and graphene, have already shown promise in such applications [62-64]. With further characterization of the effects of elevated temperatures on the materials produced in the present work, multi-material manufacturing with thermal cure polymers encased within the UV cured matrix may even be possible.

Once the ideal rheological properties of resins for use in the CFDW process have been identified for replication, other UV curable polymers and polymer composites could be introduced to provide more favorable characteristics. For example, zinc oxide and titanium dioxide particles in UV curable resins have shown the ability to both increase

printed objects' strength and water resistance, and even bestow antibacterial properties [65, 66]. This could benefit the products of CFDW in applications like high strength, low weight prosthetics. Other work has shown metal-metal oxide nanoparticles can serve to improve the thermal properties of UV curable polymers [67]. The additively manufactured composites and nanocomposites can obtain improved mechanical properties and other beneficial functionalities, such as autonomous load sensing, structural health monitoring, environmental monitoring, and energy storage [68-74].

References

[1] C. E. Bakis *et al.*, "Fiber-reinforced polymer composites for construction—State-of-the-art review," *Journal of composites for construction,* vol. 6, no. 2, pp. 73-87, 2002.

[2] S. Prashanth, K. Subbaya, K. Nithin, and S. Sachhidananda, "Fiber reinforced composites-a review," *J. Mater. Sci. Eng,* vol. 6, no. 03, pp. 2-6, 2017.

[3] D. K. Rajak, D. D. Pagar, P. L. Menezes, and E. Linul, "Fiber-reinforced polymer composites: Manufacturing, properties, and applications," *Polymers,* vol. 11, no. 10, p. 1667, 2019.

[4] T. Sathishkumar, S. Satheeshkumar, and J. Naveen, "Glass fiber-reinforced polymer composites–a review," *Journal of reinforced plastics and composites,* vol. 33, no. 13, pp. 1258-1275, 2014.

[5] S.-S. Yao, F.-L. Jin, K. Y. Rhee, D. Hui, and S.-J. Park, "Recent advances in carbon-fiber-reinforced thermoplastic composites: A review," *Composites Part B: Engineering,* vol. 142, pp. 241-250, 2018.

[6] A. Belarbi, M. Dawood, and B. Acun, "Sustainability of fiber-reinforced polymers (FRPs) as a construction material," in *Sustainability of construction materials*: Elsevier, 2016, pp. 521-538.

[7] A. Bhat, J. Naveen, M. Jawaid, M. Norrrahim, A. Rashedi, and A. Khan, "Advancement in fiber reinforced polymer, metal alloys and multi-layered armour systems for ballistic applications–A Review," *Journal of Materials Research and Technology,* vol. 15, pp. 1300-1317, 2021.

[8] J. K. Borchardt, "Unmanned aerial vehicles spur composites use," *Reinforced plastics,* vol. 48, no. 4, pp. 28-31, 2004.

[9] C. Soutis, "Fibre reinforced composites in aircraft construction," *Progress in aerospace sciences,* vol. 41, no. 2, pp. 143-151, 2005.

[10] M. Saadi *et al.*, "Direct Ink Writing: A 3D Printing Technology for Diverse Materials," *Advanced Materials,* p. 2108855, 2022.

[11] R. F. Gibson, *Principles of composite material mechanics*. CRC press, 2016.

[12] B. Berman, "3-D printing: The new industrial revolution," *Business horizons,* vol. 55, no. 2, pp. 155-162, 2012.

[13] V. Shanmugam *et al.*, "The mechanical testing and performance analysis of polymer-fibre composites prepared through the additive manufacturing," *Polymer testing,* vol. 93, p. 106925, 2021.

[14] M. Gebler, A. J. S. Uiterkamp, and C. Visser, "A global sustainability perspective on 3D printing technologies," *Energy policy,* vol. 74, pp. 158-167, 2014.

[15] J. Li, X. Huang, Y. Durandet, and D. Ruan, "A review of the mechanical properties of additively manufactured fiber reinforced composites," in *IOP Conference Series: Materials Science and Engineering*, 2021, vol. 1067, no. 1: IOP Publishing, p. 012105.

[16] P. Parandoush and D. Lin, "A review on additive manufacturing of polymer-fiber composites," *Composite Structures,* vol. 182, pp. 36-53, 2017.

[17] X. Wang, M. Jiang, Z. Zhou, J. Gou, and D. Hui, "3D printing of polymer matrix composites: A review and prospective," *Composites Part B: Engineering,* vol. 110, pp. 442-458, 2017.

[18] T. D. Ngo, A. Kashani, G. Imbalzano, K. T. Nguyen, and D. Hui, "Additive manufacturing (3D printing): A review of materials, methods, applications and challenges," *Composites Part B: Engineering,* vol. 143, pp. 172-196, 2018.
[19] M. Abshirini, P. Marashizadeh, M. C. Saha, M. C. Altan, and Y. Liu, "Three-Dimensional Printed Highly Porous and Flexible Conductive Polymer Nanocomposites with Dual-Scale Porosity and Piezoresistive Sensing Functions," *ACS Applied Materials & Interfaces,* vol. 15, no. 11, pp. 14810-14825, 2023.
[20] M. Abshirini, M. C. Saha, M. C. Altan, and Y. Liu, "3D printed flexible microscaled porous conductive polymer nanocomposites for piezoresistive sensing applications," *Advanced Materials Technologies,* vol. 7, no. 9, p. 2101555, 2022.
[21] A. Renteria *et al.*, "Particle size influence on material properties of BaTiO3 ceramics fabricated using freeze-form extrusion 3D printing," *Materials Research Express,* vol. 6, no. 11, p. 115211, 2019.
[22] M. Abshirini, M. Charara, Y. Liu, M. Saha, and M. C. Altan, "3D printing of highly stretchable strain sensors based on carbon nanotube nanocomposites," *Advanced Engineering Materials,* vol. 20, no. 10, p. 1800425, 2018.
[23] A. Renteria *et al.*, "Optimization of 3D printing parameters for BaTiO3 piezoelectric ceramics through design of experiments," *Materials Research Express,* vol. 6, no. 8, p. 085706, 2019.
[24] MakerBot. "Makerbot PLA: Rigid and glossy parts for quick and Easy Prototyping." MakerBot. https://www.makerbot.com/3d-printers/materials/method-pla/?utm_adgroup=MakerBot_PLA (accessed 20 March 2023, 2023).
[25] MakerBot. "MAKERBOT ABS: REAL, PRODUCTION- GRADE ABS FOR MANUFACTURING APPLICATIONS." https://www.makerbot.com/3d-printers/materials/method-abs/ (accessed 20 March 2023, 2023).
[26] MakerBot. "MAKERBOT NYLON: HIGH ABRASION RESISTANCE FOR INDUSTRIAL APPLICATIONS." https://www.makerbot.com/3d-printers/materials/method-nylon/ (accessed 20 March 2023, 2023).
[27] S. Sun, M. Brandt, and M. Easton, "Powder bed fusion processes: An overview," *Laser additive manufacturing,* pp. 55-77, 2017.
[28] D. D. Singh, T. Mahender, and A. R. Reddy, "Powder bed fusion process: A brief review," *Materials Today: Proceedings,* vol. 46, pp. 350-355, 2021.
[29] A. Vafadar, F. Guzzomi, A. Rassau, and K. Hayward, "Advances in metal additive manufacturing: a review of common processes, industrial applications, and current challenges," *Applied Sciences,* vol. 11, no. 3, p. 1213, 2021.
[30] W. Zhong, F. Li, Z. Zhang, L. Song, and Z. Li, "Short fiber reinforced composites for fused deposition modeling," *Materials Science and Engineering: A,* vol. 301, no. 2, pp. 125-130, 2001.
[31] MakerBot. "MAKERBOT NYLON CARBON FIBER & NYLON 12 CARBON FIBER: PRINT STRONG, HEAT-RESISTANT METAL REPLACEMENT PARTS." https://www.makerbot.com/3d-printers/materials/method-nylon-carbon-fiber/ (accessed 20 March 2023, 2023).
[32] Markforged. "Onyx™: Micro carbon fiber filled nylon that forms the foundation of Markforged composite parts."

https://markforged.com/materials/plastics/onyx (accessed 20 March 2023, 2023).
[33] F. Ning, W. Cong, J. Qiu, J. Wei, and S. Wang, "Additive manufacturing of carbon fiber reinforced thermoplastic composites using fused deposition modeling," *Composites Part B: Engineering,* vol. 80, pp. 369-378, 2015.
[34] Kimya. "Kimya ABS Carbon 3D Filament." https://www.kimya.fr/en/product/abs-carbon-3d-filament/ (accessed 20 March 2023, 2023).
[35] 3DXTECH. "FIBREX ABS+GF." https://www.3dxtech.com/product/fibrex-abs-gf/ (accessed 20 March 2023, 2023).
[36] A. V. Azarov, F. K. Antonov, M. V. Golubev, A. R. Khaziev, and S. A. Ushanov, "Composite 3D printing for the small size unmanned aerial vehicle structure," *Composites Part B: Engineering,* vol. 169, pp. 157-163, 2019.
[37] N. Li, Y. Li, and S. Liu, "Rapid prototyping of continuous carbon fiber reinforced polylactic acid composites by 3D printing," *Journal of Materials Processing Technology,* vol. 238, pp. 218-225, 2016.
[38] R. Matsuzaki *et al.*, "Three-dimensional printing of continuous-fiber composites by in-nozzle impregnation," *Scientific reports,* vol. 6, no. 1, pp. 1-7, 2016.
[39] A. Fischer, S. Rommel, and T. Bauernhansl, "New fiber matrix process with 3D fiber printer–A strategic in-process integration of endless fibers using fused deposition modeling (FDM)," in *Digital Product and Process Development Systems: IFIP TC 5 International Conference, NEW PROLAMAT 2013, Dresden, Germany, October 10-11, 2013. Proceedings*, 2013: Springer, pp. 167-175.
[40] S. Liu, Y. Li, and N. Li, "A novel free-hanging 3D printing method for continuous carbon fiber reinforced thermoplastic lattice truss core structures," *Materials & Design,* vol. 137, pp. 235-244, 2018.
[41] H. Zhang, T. Huang, Q. Jiang, L. He, A. Bismarck, and Q. Hu, "Recent progress of 3D printed continuous fiber reinforced polymer composites based on fused deposition modeling: a review," *Journal of Materials Science,* vol. 56, no. 23, pp. 12999-13022, 2021.
[42] H. Zhao, X. Liu, W. Zhao, G. Wang, and B. Liu, "An Overview of Research on FDM 3D Printing Process of Continuous Fiber Reinforced Composites," in *Journal of Physics: Conference Series*, 2019, vol. 1213, no. 5: IOP Publishing, p. 052037.
[43] C. Yang, X. Tian, T. Liu, Y. Cao, and D. Li, "3D printing for continuous fiber reinforced thermoplastic composites: mechanism and performance," *Rapid Prototyping Journal,* vol. 23, no. 1, pp. 209-215, 2017.
[44] Q. Hu, Y. Duan, H. Zhang, D. Liu, B. Yan, and F. Peng, "Manufacturing and 3D printing of continuous carbon fiber prepreg filament," *Journal of materials science,* vol. 53, pp. 1887-1898, 2018.
[45] H. Pierson *et al.*, "Mechanical properties of printed epoxy-carbon fiber composites," *Experimental mechanics,* vol. 59, pp. 843-857, 2019.
[46] J. Chen *et al.*, "3D-Printed anisotropic polymer materials for functional applications," *Advanced Materials,* vol. 34, no. 5, p. 2102877, 2022.
[47] F. Fernandez, W. S. Compel, J. P. Lewicki, and D. A. Tortorelli, "Optimal design of fiber reinforced composite structures and their direct ink write fabrication,"

Computer Methods in Applied Mechanics and Engineering, vol. 353, pp. 277-307, 2019.
[48] G. Griffini, M. Invernizzi, M. Levi, G. Natale, G. Postiglione, and S. Turri, "3D-printable CFR polymer composites with dual-cure sequential IPNs," *Polymer,* vol. 91, pp. 174-179, 2016.
[49] Y. Saito, F. Fernandez, D. Tortorelli, W. Compel, J. Lewicki, and J. Lambros, "Experimental validation of an additively manufactured stiffness-optimized short-fiber reinforced composite clevis joint," *Experimental Mechanics,* vol. 59, pp. 859-869, 2019.
[50] Y. Ming, S. Zhang, W. Han, B. Wang, Y. Duan, and H. Xiao, "Investigation on process parameters of 3D printed continuous carbon fiber-reinforced thermosetting epoxy composites," *Additive Manufacturing,* vol. 33, p. 101184, 2020.
[51] Y. Ming, Y. Duan, B. Wang, H. Xiao, and X. Zhang, "A novel route to fabricate high-performance 3D printed continuous fiber-reinforced thermosetting polymer composites," *Materials,* vol. 12, no. 9, p. 1369, 2019.
[52] M. A. Rahman, M. Z. Islam, L. Gibbon, C. A. Ulven, and J. J. La Scala, "3D printing of continuous carbon fiber reinforced thermoset composites using UV curable resin," *Polymer Composites,* vol. 42, no. 11, pp. 5859-5868, 2021.
[53] X. He *et al.*, "3D printing of continuous fiber-reinforced thermoset composites," *Additive Manufacturing,* vol. 40, p. 101921, 2021.
[54] R. Cowdrey, "Manufacturing of Continuous Carbon Fiber Composites Using Ultraviolet Laser-Assisted Direct Ink Write 3D Printing," 2020.
[55] Arkema. "Technical Data Sheet: PR48-Clear Clear Prototyping Material." CPSPolymers. https://cpspolymers.com/PR48%20TDS.pdf (accessed 20 March 2023, 2023).
[56] I. Toray Composite Materials America. "T300 Standard Modulus Carbon Fiber." https://www.toraycma.com/wp-content/uploads/T300-Technical-Data-Sheet-1.pdf.pdf (accessed 20 March 2023, 2023).
[57] BYK. "GARAMITE-1958." https://www.byk.com/en/products/additives-by-name/garamite-1958 (accessed 20 March 2023, 2023).
[58] E. Foundation. "IGES file Specification." https://wiki.eclipse.org/IGES_file_Specification#Line_.28Type_110.29 (accessed 20 March 2023, 2023).
[59] A. ASTM, "D3039 Standard test method for tensile properties of polymer matrix composite materials," *ASTM International: West Conshohocken, PA, USA,* 2017.
[60] A. ASTM, "D3171-22 Standard Test Methods for Constituent Content of Composite Materials," *ASTM International: West Conshohocken, PA, USA,* 2022.
[61] V. G. Rocha, E. Saiz, I. S. Tirichenko, and E. García-Tuñón, "Direct ink writing advances in multi-material structures for a sustainable future," *Journal of Materials Chemistry A,* vol. 8, no. 31, pp. 15646-15657, 2020.
[62] B. Herren, M. C. Saha, M. C. Altan, and Y. Liu, "Development of ultrastretchable and skin attachable nanocomposites for human motion monitoring via embedded 3D printing," *Composites Part B: Engineering,* vol. 200, p. 108224, 2020.

[63] Y. Liu and S. Nayak, "Structural health monitoring: State of the art and perspectives," *Jom,* vol. 64, no. 7, pp. 789-792, 2012.
[64] A. Renteria *et al.*, "Direct ink write multi-material printing of PDMS-BTO composites with MWCNT electrodes for flexible force sensors," *Flexible and Printed Electronics,* vol. 7, no. 1, p. 015001, 2022.
[65] C. Billings, C. Cai, and Y. Liu, "Utilization of antibacterial nanoparticles in photocurable additive manufacturing of advanced composites for improved public health," *Polymers,* vol. 13, no. 16, p. 2616, 2021.
[66] C. Billings, P. Kim, T. Shadid, J. D. Ballard, C. Cai, and Y. Liu, "Implementation of Antibacterial Nanoparticles in Additive Manufacturing to Increase Part Strength and Stiffness," *Journal of Composites Science,* vol. 6, no. 9, p. 248, 2022.
[67] S. Mubarak *et al.*, "A novel approach to enhance mechanical and thermal properties of SLA 3D printed structure by incorporation of metal–metal oxide nanoparticles," *Nanomaterials,* vol. 10, no. 2, p. 217, 2020.
[68] A. M. Alsharabasy, A. Pandit, and P. Farràs, "Recent advances in the design and sensing applications of hemin/coordination polymer-based nanocomposites," *Advanced Materials,* vol. 33, no. 2, p. 2003883, 2021.
[69] J. ZOU, Y. LIU, A. CHATTOPADHYAY, and L. DAI, "Self-sensing of Matrix Damage using Mechanophore-based Smart Polymer in Fiber Reinforced Composites," *Journal of Multifunctional Composites,* vol. 2, pp. 207-215, 2014.
[70] Y. Liu, S. B. Kim, A. Chattopadhyay, and D. Doyle, "Application of system-identification techniquest to health monitoring of on-orbit satellite boom structures," *Journal of Spacecraft and Rockets,* vol. 48, no. 4, pp. 589-598, 2011.
[71] Y. Liu, S. Mohanty, and A. Chattopadhyay, "Condition based structural health monitoring and prognosis of composite structures under uniaxial and biaxial loading," *Journal of Nondestructive Evaluation,* vol. 29, pp. 181-188, 2010.
[72] Y. Liu, M. Y. Fard, A. Chattopadhyay, and D. Doyle, "Damage assessment of CFRP composites using a time–frequency approach," *Journal of Intelligent Material Systems and Structures,* vol. 23, no. 4, pp. 397-413, 2012.
[73] S. Das, B. Sen, and N. Debnath, "Recent trends in nanomaterials applications in environmental monitoring and remediation," *Environmental Science and Pollution Research,* vol. 22, pp. 18333-18344, 2015.
[74] A. U. Agobi, H. Louis, T. O. Magu, and P. M. Dass, "A review on conducting polymers-based composites for energy storage application," *J. Chem. Rev,* vol. 1, no. 1, pp. 19-34, 2019.